공학석사 학위논문

Glass-forming ability and mechanical responses in a series of equiatomic binary to denary metallic glasses

엔트로피 제어 비정질 형성 합금 시스템에서 비정질 형성능 및 기계적 특성 변화 고찰

2019 년 8 월

서울대학교 대학원
재료공학부
이 정 수

Abstract

Glass–forming ability and mechanical responses in a series of equiatomic binary to denary metallic glasses

Jung Soo Lee

Department of Materials Science and Engineering

College of Engineering

Seoul National University

Herein, we systematically investigated the effect of configuration entropy (CE) on the glass–forming ability (GFA) and the mechanical response in a series of equiatomic binary $Cu_{50}Zr_{50}$ to denary $(CuNiBeCoFe)_{50}(ZrTiHfTaNb)_{50}$ metallic glasses (MGs) with similar atomic size difference and heat of mixing through alloy design involving careful selection of elements chemically and topologically similar to Cu and Zr and subsequent substitution of pre–constituent elements. Interestingly, the senary $(CuNiBe)_{50}(ZrTiHf)_{50}$ MG with relatively medium CE value of $1.79R$ exhibited the maximum GFA among the investigated MGs, implying that the CE is not the dominant factor for GFA. The mechanical response analysis was comprehensively performed using nanoindentation test including deformation dynamics of shear avalanche through statistical analysis

of pop-in behavior and the analysis result was compared to the atomic-level structure data obtained by high energy X-ray scattering experiment. The overall trend of the nanohardness and the Young's modulus (E) was shown to outwardly increase which is dominantly due to the increased 3 atom-connection of polyhedra as well as lower fragility. However, the severe local structural irregularity and compositional complexity in MG with higher CE facilitate the chaotic deformation behavior that results in the unanticipated local softening of amorphous phase and ultimately modulate the response towards ductile deformation. Consequently, it can be concluded that the CE could be one of the crucial factors in designing an MG to alter its characteristics towards achieving desirable properties such as optimized GFA and enhanced ductility.

Keywords: Metallic glass; Configuration entropy; Glass-forming ability; Local structural irregularity; Mechanical response

Student number: 2017-25308

Table of Contents

List of Figures

List of Tables

Chapter 1. Introduction

1.1. Metallic glass

1.1.1. Definition and charactersitics

Metallic glasses are amorphous structured metallic materials usually in alloy form as schematically shown in Fig. 1.1. MGs being non-crystalline in nature, they are devoid of defects such as vacancy, dislocation and grainboundary that are closely related to the deformation mechanism. Such structural dissimilarity brings out novel properties of MGs significantly different from crystalline metals. They show higher yield strengths, elastic strain limits, wear and corrosion resistance, but exhibit severely lower ductility than the crystalline counterparts [1].

MGs can be fabricated via various processing methods available but the most widely used is the rapid solidification processing route. In this method, the alloy melts are rapidly solidified usually at the cooling rates greater than 10^6 K/s, maintaining the amorphous structure possessed by the liquid. Fundamentally, the amorphous phase can be frozen and brought down the lower temperatures by rapid quenching the liquid melt at cooling rates sufficiently high enough to avoid onset of nucleation which is represented by the C-curve from the time-temperature-transformation plot. Depending on the critical cooling rate of the alloy, the maximum or critical diameter

with which the alloy can be produced into a glass differs. The alloys that are able to form glasses with higher critical diameters are said to exhibit better GFA. Generally, alloys which possess critical diameters equal to or greater than 1 mm is considered as bulk metallic glasses (BMGs) [1].

Empirically, the better glass formers satisfied the following conditions [2]. (1) multicomponent system bearing three or more elements, (2) atomic size difference greater than 12% among constituent elements and (3) negative (less than −12 kJ/mol) heat of mixing.

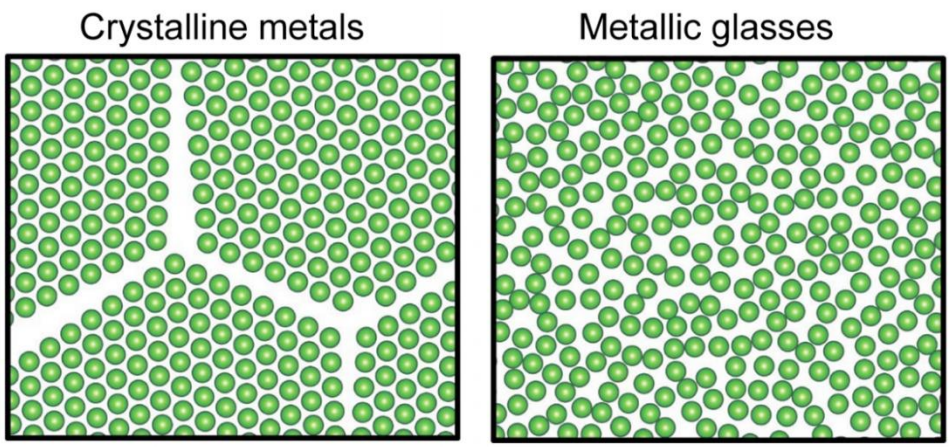

Figure 1.1. Schematic diagram depicting the atomic arrangement in crystalline metals and metallic glasses [3].

1.1.2. Glass-forming ability parameter

Although the critical diameter and the critical cooling rate is the absolute measure of GFA of an alloy, several parameters were proposed to easily evaluate and predict the GFA without actually determining the critical diameter and the cooling rate that require tedious experiments.

The most basic yet effective parameter is the reduced glass transition temperature (T_{rg}) [4]. It is calculated by the following equation

$$T_{rg} = \frac{T_g}{T_l} \qquad \text{eq. 1.1}$$

Where, T_g is the glass transition temperature and T_l is the liquidus temperature. Conceptually, higher value of T_{rg} implies slower nucleation and growth of the crystalline phase allowing slower cooling rates to maintain the glassy state.

Another widely used parameter is the γ parameter that is calculated by the equation shown below [5]

$$\gamma = \frac{T_x}{T_g + T_l} \qquad \text{eq. 1.2}$$

Where, T_x is the crystallization temperature. This parameter is powerful in the sense that it simultaneously considers the thermodynamic and kinetic aspects of glass formation. This can be understood with the help of the time-temperature-transformation

(TTT) plot in Fig. 1.2. The denominator term $(T_g + T_l)$ is correlated to the average value of the liquidus and the glass transition temperature where lower value would mean better thermodynamic liquid stability even at lower temperatures which would yield better GFA. And the crystallization temperature at the numerator represents the resistance to crystallization that considers the kinematic aspect as alloys harder to crystallize would have their C−curve towards the right hand side leading the higher crystallization temperatures for a specific heating rate from room temperature.

ε parameter is a relatively newly developed parameter that is also based on the combination of thermodynamic and kinetic aspects obtained by the following equation [6]

$$\varepsilon = \frac{(\Delta T_m + \Delta T_x + T_x)}{T_m^{mix}} \qquad \text{eq. 1.3}$$

$$\Delta T_m = T_m^{mix} - T_l \qquad \text{eq. 1.4}$$

$$\Delta T_x = T_x - T_g \qquad \text{eq. 1.5}$$

Where, T_m^{mix} is the rule of mixture melting temperature of constituent elements. The numerator has a special physical meaning. When the quantity is subtracted from the T_m^{mix}, it represents the width of the C−curve at a particular time equivalent to the time taken to crystallize by heating the MG. The Fig.1.3 schematically helps to understand the physical significance of the parameter visually. The smaller the width of the C−curve or larger the numerator in the eq.

1.3, longer is the time needed for the crystallization onset.

A common feature of the aforementioned GFA parameters is that they can simply be obtained by characteristic temperatures of constituent elements and the alloy which can relatively easily be found in the literature or by calorimetry techniques. However, one should note that the values of the parameters gives us the idea on the relative GFA and is not the absolute quantity of measurement.

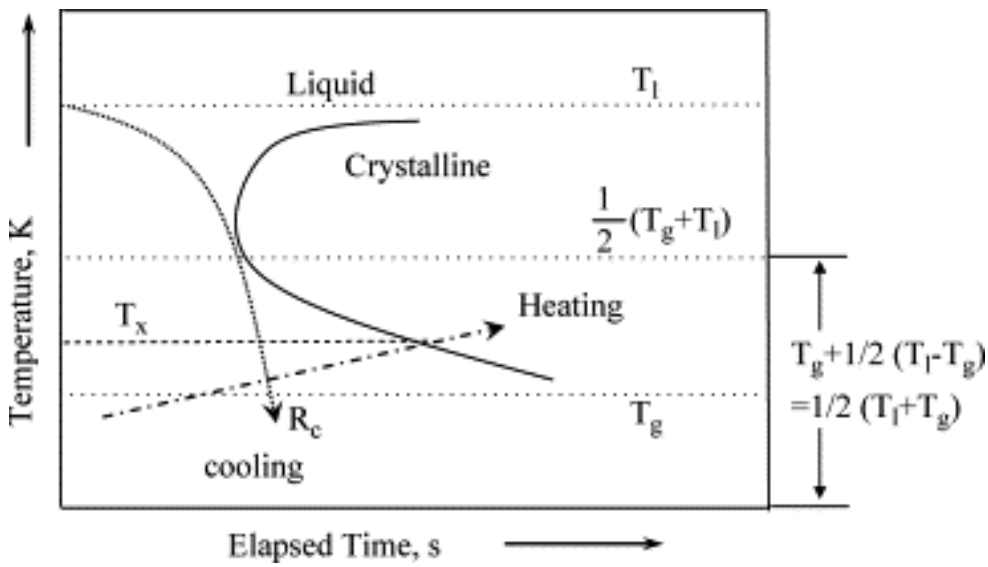

Figure 1.2. Schematic illustration of TTT diagram showing the physical meaning behind the γ parameter. Reused from [5] with permission through "Copyright Clearance Center".

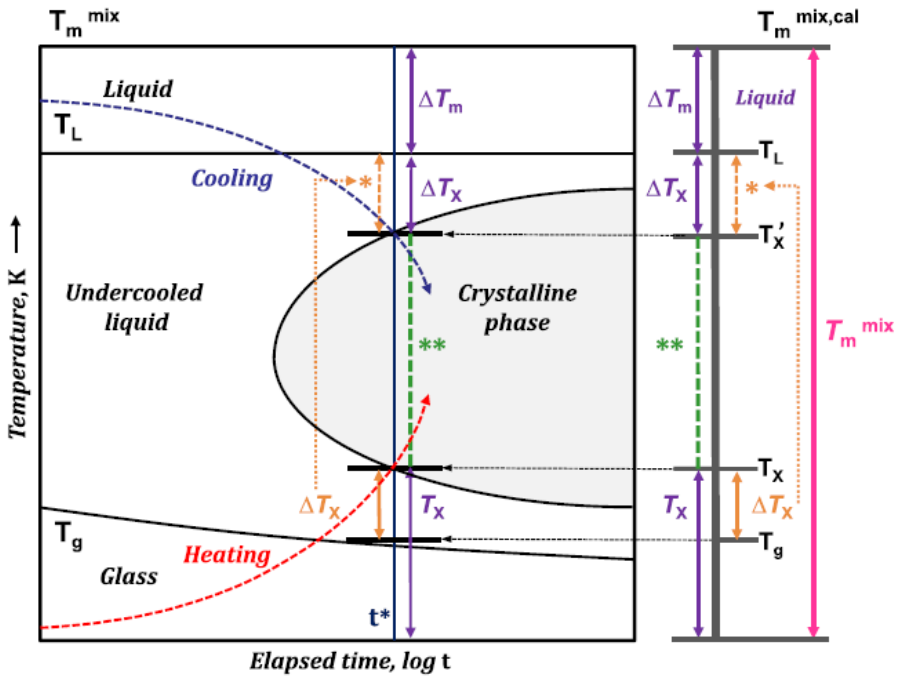

Figure 1.3. Schematic illustration of TTT diagram showing the physical meaning behind the ε parameter. Reused from [6] with permission through "Copyright Clearance Center".

1.1.3. Fragility

Fragility is described as an indicator of how sensitive the structure of the liquid is to temperature changes [1]. The fragility index can be expressed as follows

$$m = \left[\frac{d \log x}{d(T_g/T)}\right]_{T=T_g} \qquad \text{eq. 1.6}$$

Where, x can be dynamic variables such as relaxation time, viscosity, etc. According to Angell [7], a liquid can be categorized as either strong or fragile depending on the variation of its viscosity with temperature. A strong glass is known to have high viscosity. This implies that the atomic movement of the liquid is slower, consequently giving rise to better GFA. Structural wise, they are more topologically densely packed, possess less free volume or potential STZ activation site that aids plastic deformation ultimately causing more brittle behavior. On the other hand, a fragile glass has the opposite characteristics i.e., lower viscosity, topologically loosely packed, have more free volume and are more ductile.

The observation of glass transition dynamics by relaxation of viscosity and the calorimetric technique are in the same time scale. Hence, employing calorimetry technique for varying heating rates with dependent glass transition dynamics helps us to calculate the dynamic fragility. Using Vogel–Fulcher–Tammann (VFT)–type function, the relationship between T_g and Φ (heating rate) can be

fitted as follows [8]

$$\ln \Phi = \frac{\ln A + D \cdot T_g^0}{\left(T_g^0 - T_g\right)} \qquad \text{eq. 1.7}$$

Where, D and T_g^0 are the fitting parameters. Once these parameters are obtained, they can be used in the equation below for the determination of the dynamic fragility

$$m = \frac{D \cdot T_g \cdot T_g^0}{\ln 10 \, (T_g - T_g^0)^2} \qquad \text{eq. 1.8}$$

Usually, the m is calculated for the T_g corresponding to the heating rate of 20 K/min.

1.1.4. Deformation mechanism

MGs being amorphous in nature, their deformation mechanisms are not dictated by the conventional defects well known in crystalline materials. Hence, their deformation is carried out by local atomic rearrangements manifested as a results of repetitive breakage and rebinding of atomic bonds [9, 10]. The local regions of deformation is referred to as the shear transformation zones (STZs) that consists of tens to hundreds of atoms overcoming potential energy barriers through collective rearrangement [10, 11] as illustrated in Fig. 1.4. Since STZs involve the movement of atoms in an extremely specific local regions, they are activated at preferential loosely packed regions where diffusion of atoms is more favorable [10]. Unlike dislocations that lower the critical stress level for the plastic deformation in conventional crystalline materials, the activation of STZs require large amount of energy [9]. This leads to higher yield strength compared to their crystalline counterparts.

The strain accommodation in MGs takes place through shear band formation with the typical thickness of tens of nanometers [9]. Essentially, the shear bands are formed via percolation of STZs. Therefore, the homogeneous distribution and activation of STZs induces more deformation at macro-scale before catastrophic failure. On the other hand, fewer shear band initiation and propagation at larger scales leads to limited deformability.

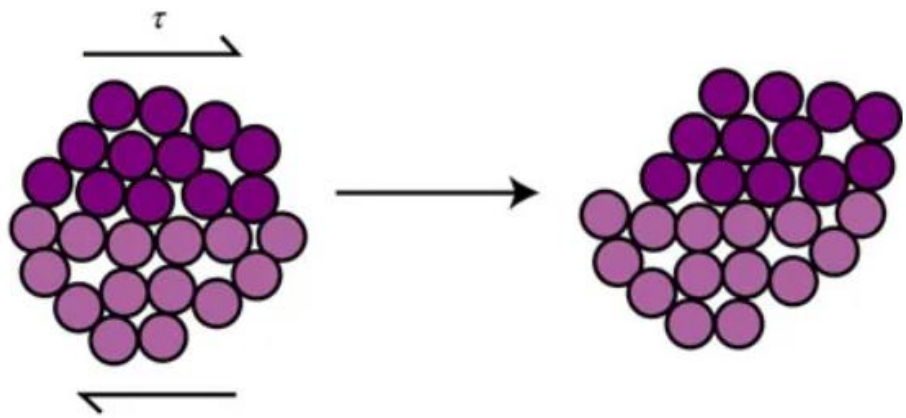

Figure 1.4. Schematic diagram of STZ undergoing atomic arrangement under the applied shear stress. Reused from [12] with permission through "Copyright Clearance Center".

1.1.5. Shear avalanche in metallic glass

Shear avalanche is defined as the spatiotemporal dynamic event where sudden accumulation of plastic strain and elastic reloading in a repeated cycle that is attributed to the shear band initiation, propagation and arrest [13, 14]. The phenomenon being spatiotemporal dynamic event, the local and overall structure of the glass and the external driving rates influence it [14]. Several investigations on shear avalanche analysis in MGs have been carried out using uniaxial compression or nanoindentation tests correlating the behavior of the shear avalanche to the mechanical properties such as ductility and the hardness of the corresponding MGs [14–17]. Fig. 1.5 shows the pop–in phenomenon manifested during nanoindentation of MGs.

In the case of analysis via nanoindentation, an explanation for the shear avalanche using a cumulative probability distribution analysis described by a truncated power–law function of strain burst sizes has been made showing that the cut–off strain burst size is lower for softer glasses since they are able to withstand lower stress level which results in manifestation of smaller pop–in events [8, 14, 18]. These MGs cannot maintain self–organized critical (SOC, jamming state of group of atoms concordantly shifting known as concordant regions) behavior and thereby yield chaotic behavior (unjamming state of concordant regions). However, such chaotic

behavior of shear avalanche can facilitate in macroscopic plastic deformation through formation of smaller shear banding events occurring more frequently. Relating the deformation dynamics information to other relevant data such as structural information could provide us deeper insights to understand them better.

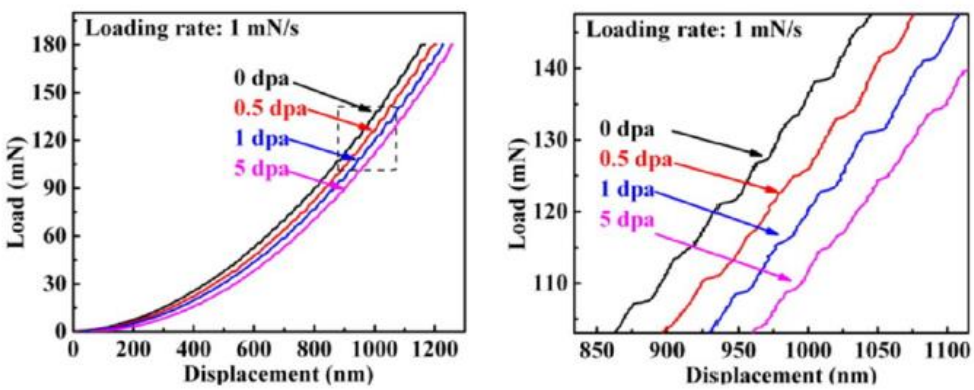

Figure 1.5. Nanoindentation loading plot of metallic glasses with pop-ins indicated by arrows manifested from the shear avalanche during the plastic deformation. Reused from [17] with permission through "Copyright Clearance Center".

1.2. High entropy alloy

1.2.1. Definition and charactersitics

In general, formation of various phases, inclusive of intermetallic phase is the common notion for multi-principal component alloys. However, in 2004, new concept of advanced material named high entropy alloy (HEA) was proposed and attracted the attention of several researchers around the globe [19, 20]. HEAs are defined as multicomponent alloys bearing more than 4 principal elements with atomic compositions of 5 to 35% each [21]. Its name is derived from the high configuration entropy condition generated from the (near-)equiatomic multicomponent composition. Even though these alloys bear multi-principal components, they are able to form simple single FCC or BCC phase microstructures.

The reason these alloys caught the attention is because they have potentially desirable properties. So far, several alloy systems have been reported to exhibit properties surpassing that of the conventional alloys. For instance, the popular CoCrFeMnNi also known as Cantor alloy was found to exhibit good low-temperature mechanical properties and high fracture toughness [22], $Al_{0.5}$CoCrCuFeNi was reported to have high fatigue life and endurance limit [23], and refractory VNbMoTaW showed high yield strength (greater than 600 MPa)at 1,400 ℃ [24].

Similar to MGs, empirical simple disordered solid solution

formation criterion was formed defined by ΔH_{mix} (heat of mixing) and δ (atomic size misfit) parameters [25]: ΔH_{mix} greater than −15 kJ/mol and δ smaller than 6%. Fig. 1.6 shows the ΔH_{mix} vs δ plot showing the regions of solid solution formation. These parameter limits are opposite to the formation criteria for BMGs which have limits of ΔH_{mix} less than −15 kJ/mol and δ greater than 6%.

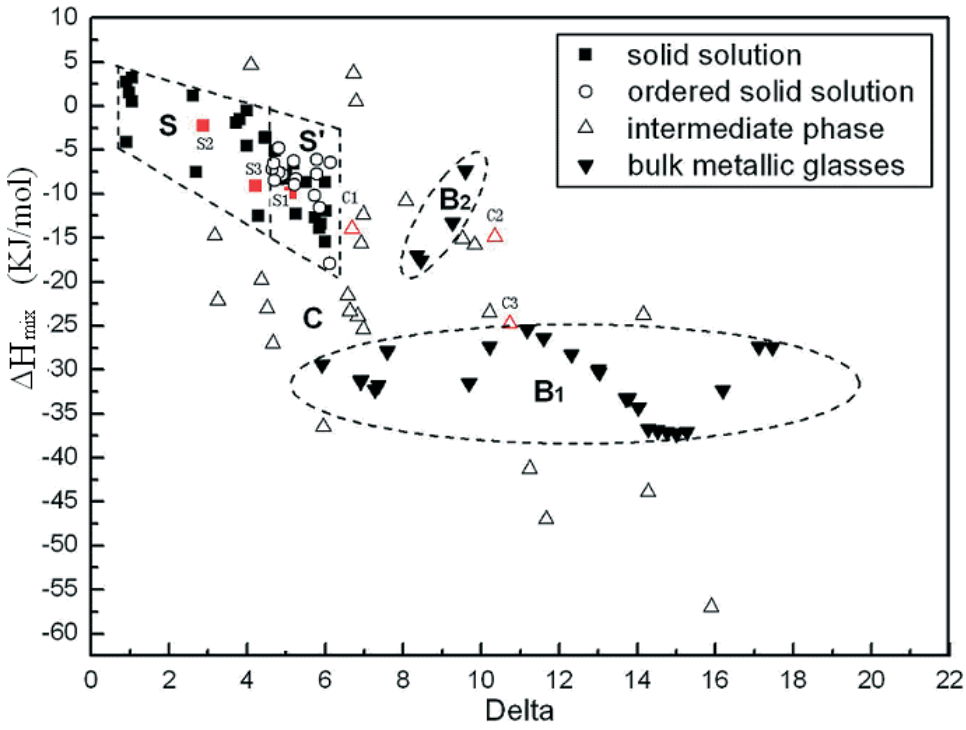

Figure 1.6. ΔH_{mix} vs δ plot showing empirically obtained regions of HEA solid solution and BMG formation. Reused from [25] with permission through "Copyright Clearance Center".

1.2.2. Four core effects of HEA

HEAs are known to possess different basic effects arising from distinct alloy design. They are (1) high-entropy, (2) severe lattice distortion, (3) sluggish diffusion, and (4) cocktail effects [21].

The high-entropy effect is the most basic and important one since it can facilitate the solid solution formation. Fundamentally, this effect is put forth by considering the Gibbs free energy of mixing (ΔG_{mix})

$$\Delta G_{mix} = \Delta H_{mix} - T\Delta S_{mix} \qquad \text{eq. 1.9}$$

Where, T is the temperature and ΔS_{mix} is the entropy of mixing. According to the equation above, at higher temperatures, larger ΔS_{mix} generated by bearing more number of elements will significantly be able to lower the ΔG_{mix}. In this way, the ordered phase with lower entropy due to its ordered nature could have higher free energy than the disordered phase, effectively leading to manifestation of the latter phase.

The severe lattice distortion effect is essentially brought by the multicomponent matrix of the alloy where the surrounding of each atom will most likely differ from the other through different element occupying the neighboring lattice sites. Although the atoms of different elements align themselves to produce a lattice structure with an average lattice parameter, the undeniable existence of atomic size difference, different bonding energy and the viable crystal

structure among constituent elements are expected to contribute to the lattice distortion. Fig. 1.7 illustrates the stage wise lattice distortion schematically from pure Cr to Al, Ni, Cr, Fe, Co, and Ti alloy. The effect would affect various properties of the alloy through the strain induced into the lattice such as inducing higher hardness by larger solution hardening.

Basically, diffusion in a material takes place by movement of a vacancy. For a conventional dilute solid solution alloy, a vacancy will most likely be surrounded by the same atom all around. However, in case of the HEA, a vacancy is surrounded different-element atoms and its diffusion will be competed by those different-element atoms. As a consequence, sluggish diffusion effect was proposed where higher activation energy would be required for the diffusion to occur due to the larger fluctuation of lattice potential energy among the lattice sites ultimately resulting in slower diffusion.

Last but not least, the cocktail effect in HEA emphasizes on the improvement of the properties that is brought by the synergetic effect of the multiple constituent elements. While the biggest characteristic of HEA is the single phase formation, careful alloy design that develops more than one phase could have better properties. In addition, each phase could be thought as a multicomponent solid solution atomic-scale composite.

.

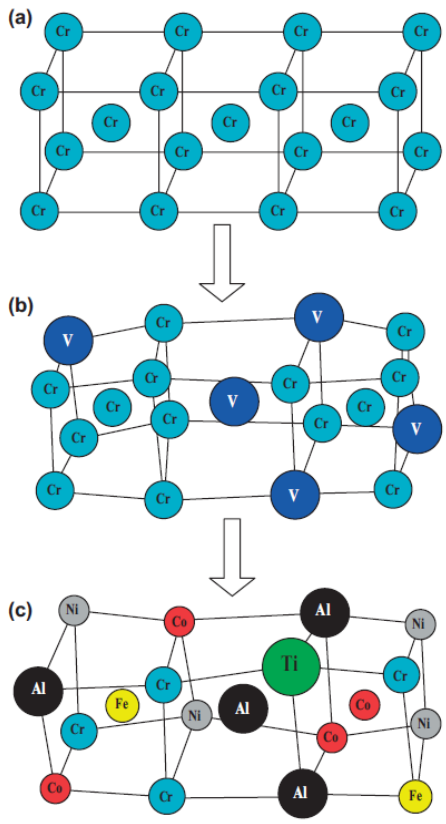

Figure 1.7. Schematic illustration of body-centered cubic structure showing the lattice distortion as pure Cr is alloyed with other metallic elements. Reused from [25] with permission through "Copyright Clearance Center".

1.3. High entropy metallic glass

Previous sections have briefly explained the features and their alloy design criteria of MGs and HEAs. As could be observed, their characteristics and properties significantly differ. However, they are developed considering the same factors, namely, number of elements, δ, and ΔH_{mix}. Therefore, designing an alloy encompassing the characteristics of both the materials can be perceived; alloys bearing more than 4 principal elements with atomic compositions of 5 to 35% each simultaneously possessing amorphous matrix. They are called as the high entropy metallic glasses (HE-MGs). As an extension, HE-MGs having critical diameters in more than 1 mm are known as high entropy bulk metallic glasses (HE-BMGs).

The alloy design of HE-MGs typically involves substitution of constituent elements with a chemically similar element from a prototypical MGs usually with good GFA since it is highly composition sensitive. For example, $Pd_{20}Pt_{20}Ni_{20}Cu_{20}P_{20}$ was derived from $Pd_{40}Ni_{40}P_{20}$ [26] . Although the method of substitution was a success, the critical diameter reduced from 25 mm to 10 mm. The conventional method for searching the optimized GFA composition is to locate the eutectic composition. However, in case of multi-principal element bearing systems like HE-MGs, the construction of fairly accurate phase diagrams are challenging and difficult due to the lack of the databases. Nevertheless, the acquisition of information and data of

various systems are actively ongoing, that will pave way for efficient alloy designing of high entropy materials as a whole from the thermodynamic perspective.

Meanwhile, since these new class of materials are based on two distinct yet uniquely advanced materials, possibly unprecedented properties arising from the combination of the characteristics of the MG and HEA are anticipated.

1.3.1. Properties and the current understanding

As HE-MGs were developed only recently, there are relatively less number of published composition and data which encourages more researches to better understand them. Nonetheless, several reports were published, presenting the positive results on the enhancements of the properties over the counterparts. $Ti_{20}Zr_{20}Cu_{20}Ni_{20}Be_{20}$ HE-BMG showed improved yield strength of over 2 GPa compared to non-equiatomic Ti-Zr-Cu-Ni-Be BMGs [27]. Studies experimentally proved better thermal stability with slower crystallization kinetics for Zr-Ti-Hf-Cu-Ni-Be and Er-Gd-Y-Al-Co HE-BMGs [8, 28]. Fig. 1.8 shows the continuous heating transformation diagram of conventional Vitreloy 1, and equiatomic HE-BMGs based on the similar constituent elements. Clearly, the HE-BMGs exhibit slower crystallization kinetics under heating condition. $Ca_{20}Mg_{20}Zn_{20}Sr_{20}Yb_{20}$ HE-BMG showed its

potential as a bio-material by possessing low Young's modulus value close to that of the cortical bone and enhanced corrosion resistance [29]. Fig. 1.9 shows the property comparison of the developed HE-BMG to BMGs of other similar compositions, proving its potential as a bio-material in mechanical and corrosion aspects. $Fe_{25}Co_{25}Ni_{25}(B,Si)_{25}$ not only showed superior soft magnetic property but also excellent yield strength of over 3 GPa and large plastic strain of about 3% [30]. These promising enhancement in properties were attributed to effects such as high degree of amorphicity & homogeneity, complex interatomic interaction and bonding, and core effects of HEA (sluggish diffusion & cocktail effect).

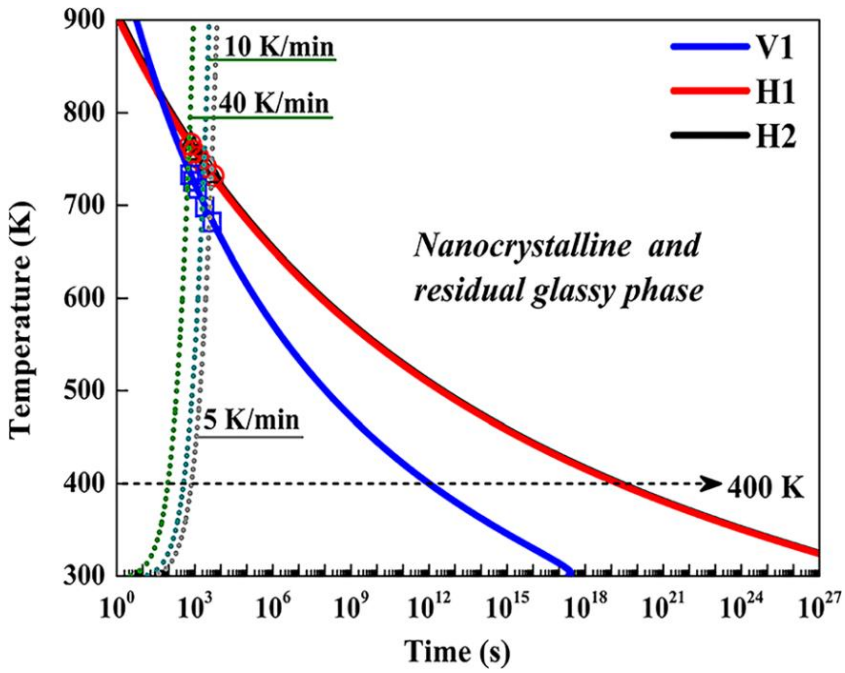

Figure 1.8. Continuous heating transformation diagrams indicating boundaries of primary precipitation for Vitreloy 1 (V1), and HE-BMGs (H1 & H2) based on the similar constituent elements. Reused from [28] with permission through "Copyright Clearance Center".

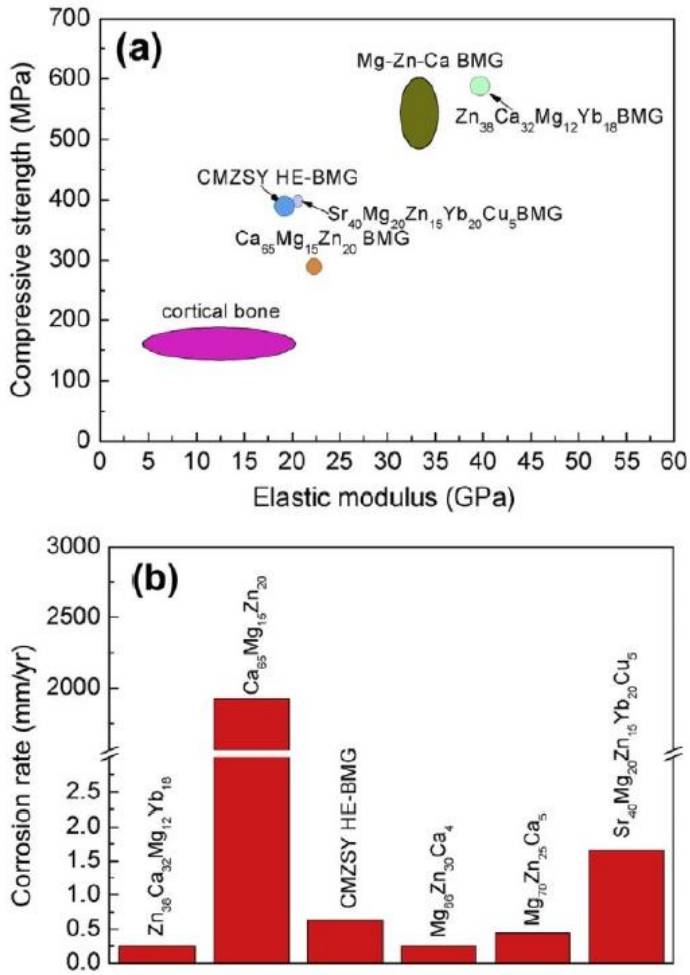

Figure 1.9. Comparison of (a) mechanical properties and (b) corrosion rate of $Ca_{20}Mg_{20}Zn_{20}Sr_{20}Yb_{20}$ (CMZSY) HE-BMG to other degradable BMGs. Reused from [29] with permission through "Copyright Clearance Center".

1.4. Thesis objective and research strategy

Previous investigations metioned in the preceding section presented various instances of HE-MGs possessing better and enhanced properties compared to their conventional MG counterparts. This certainly shows better application potential over the counterparts. However, the previous investigations mainly attributed the property improvement to the core effects of HEA and little attention has been focused on the effect of configuration entropy on the properties of MGs. Understanding the effect of configuration entropy could play a crucial role in comprehending HE-MGs better which can have implications for new alloy designs.

Therefore, the objective of this work is to systematically investigate the effect of configuration entropy on the GFA and the mechanical responses. To effectively proceed with this research, strategy planning was done as follows

1) To minimize the effect of parameters that influence the properties of MG: develop series of new alloy systems through careful selection of constituent elements with minimum ΔH_{mix} and δ deviation.
2) To assess the effect of configuration entropy on the GFA: evaluate and compare the GFA parameters through determination and analysis of thermal properties.
3) Elucidate on the influence of configuration entropy on the

deformation dynamics: perform shear-avalanche statistical analysis of pop-in behavior and correlate the mechanical response to the atomic-level structure.

To satisfy the requirements of the research plan, first, based on the topological and chemical aspect of elements, a series of equiatomic binary $Cu_{50}Zr_{50}$ to denary $(CuNiBeCoFe)_{50}(ZrTiHfTaNb)_{50}$ MGs were considered. Then, differential scanning calorimetry was carried out to evaluate the characteristic temperatures of the alloys to determine their GFA parameters. Finally, nanoindenter was employed for the mechanical testing to perform analysis of pop-in behavior and high energy X-ray scattering was perfomed for the quatlitative analysis of the atomic-level structure of the investigated alloys. This detailed analysis of atomic-level structure provided information in interpreting the mechanical response data.

Chapter 2. Experimental procedure

2.1. Sample preparation

2.1.1. Fabrication of metallic glass ribbon

Master alloy ingots of $Cu_{50}Zr_{50}$, $(CuNi)_{50}(ZrTi)_{50}$, $(CuNiBe)_{50}(ZrTiHf)_{50}$, $(CuNiBeCo)_{50}(ZrTiHfTa)_{50}$, $(CuNiBeCoFe)_{50}(ZrTiHfTaNb)_{50}$ (in at.%) were prepared by arc-melting high purity (>99.9%) Cu, Ni, Be, Co, Fe, Zr, Ti, Hf, Ta, and Nb under Ti-gettered argon atmosphere. The ingots were re-melted at least four times to ensure chemical homogeneity. Thereafter, melt spinning technique was employed to produce ribbon specimens, where the ingots were re-melted using an induction heater in quartz tubes and were quickly ejected with an over-pressure of 50 kPa through a 1 mm-diameter circular nozzle onto a copper wheel rotating with the surface velocity of approximately 40 m/s.

2.2. Structural analysis

2.2.1. X-ray diffraction

The amorphous structure of the as-spun ribbon specimens were confirmed in theta-2theta configuration from 20 ° to 80 ° with a step size of a scanning rate of 0.03 °/sec by X-ray diffraction (XRD; Bruker D2 Phaser) using monochromatic Cu Kα radiation at applied voltage of 30 kV and current of 10 mA.

2.2.2. Transmission electron microscopy

The microstructure of the as-spun ribbon specimens were examined using transmission electron microscopy (TEM) technique. The thin TEM foil specimens were prepared by mechanical polishing and Ar ion milling (Gatan PIPS II model 695) at 3.0 keV under LN_2 cooling. High-resolution TEM (Thermo Fisher Scientific Titan 80-300, shown in Fig. 2.1) with the acceleration voltage of 300 keV. Intensity profile is calculated from SAD pattern using the Gatan Digital Micrograph software with the PASAD-tools [31].

2.2.3. High energy X-ray scattering

For the detailed analysis on the local atomic structure, high energy X-ray scattering (XRS) was carried out at room temperature

at the 6-ID-D beam line of the Advanced Photon Source, Argonne National Laboratory (shown in Fig. 2.2), using monochromatic X-ray beam with the wavelength of 0.123686 Å (corresponding energy of ~100 keV) in transmission mode. A two-dimensional stationary detector comprised of 2048 × 2048 pixels with each pixel size of 200 μm × 200 μm was employed. Calibration of the beam center, detector tilt angles and the distance between the sample and the detector was carried out using CeO_2 powder. Correction of the dark current and re-binning of the data were performed using FIT2D software [32]. PDFgetX2 software [33] was utilized to generate the radial distribution function, denoted as **g(r)**, from the high energy XRS data by correcting the background and the Compton scattering, and subsequently through Fourier transformation.

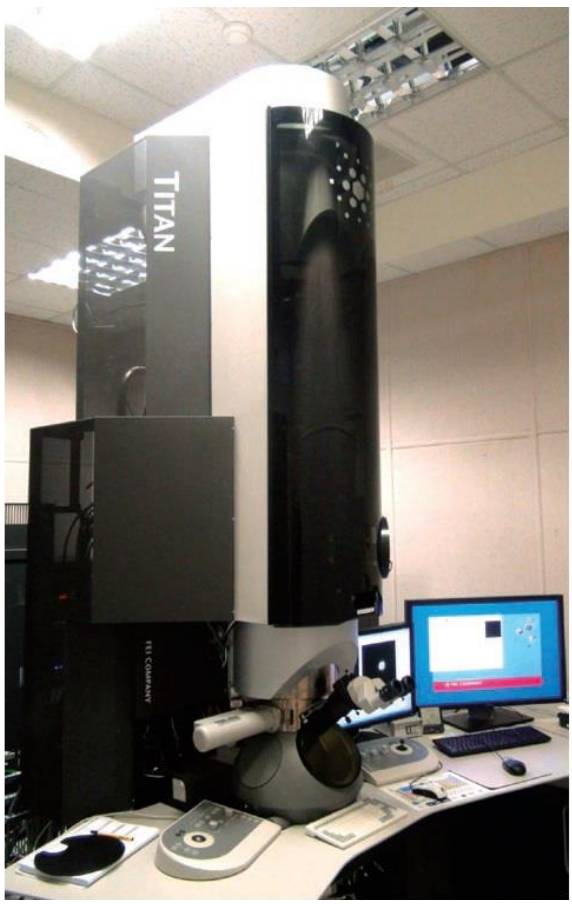

Figure 2.1. High-resolution TEM (Thermo Fischer Scientific Titan 80-300)in Korea Institute of Science and Technology [34].

Figure 2.2. Photo taken at Advanced Photon Source beamline 6-ID-D showing the beam outlet and the detector.

2.3. Thermal analysis

2.3.1. Differential scanning calorimetry

Thermal analysis was carried out during contitnuous heating with various heating rates of 10, 20, 40, 80, and 160 K/min to determine the T_g and the T_x of as-spun ribbon specimens in Cu pans using differential scanning calorimeter (Perkin Elmer DSC 8500) up to the maximum measurable temperature of 680 ℃ in Ar gas atmosphere.

Measurement at higher temperatures for T_l was done using another DSC equipment (Mettler Toledo 1 STARe system), placing the samples in Al_2O_3 crucibles at heating rate of 40 K/min in Ar gas atmosphere.

2.4. Mechanical testing

2.4.1. Nanoindentation test

Quasi-static nanoindentation was performed using Hysitron TI 750 Triboindenter (shown in Fig. 2.3) with a 2 μm radius conical type indenter at least 100 times for each alloy composition. Maximum indentation force of 8 mN was reached in 40 s, held for 2 s, and was withdrawn in 5 s at constant loading rates. The obtained load vs depth curves were fitted to a second degree polynomial equation and were subtracted by the fitted curve to easily distinguish the pop-ins. A MATLAB based code was used to appropriately determine the noise level from the holding time signal that contain the instrumentally generated noise in order to identify the small pop-in like features. Further processing was performed to calculate the strain burst sizes of each pop-ins and analyze the shear avalanche deformation dynamics using the cumulative probability distribution function.

Figure 2.3. Nanoindenter (Hysitron TI 750 Triboindenter) used for the mechanical testing [35].

Chapter 3. Result

3.1. Alloy design

In order to investigate the effect of configuration entropy on the properties of MGs, ΔH_{mix} and δ deviation had to be kept at a minimum. So, the alloy design was built up around from an equiatomic binary alloy, subsequently substituting the constituent elements with other topologically and chemically similar elements whilst maintaining the equiatomic ratio to achieve the high configuration entropy condition. Cu–Zr binary alloy system is a well–known popular system that exhibits good GFA for wide range of compositions where $Cu_{50}Zr_{50}$ alloy shows critical diameter of 2 mm [36]. By carefully selecting the elements similar to Cu and Zr from the periodic table, we can narrow down the list to Ni, Be, Co, and Fe for Cu and Ti, Hf, Ta, and Nb for Zr. Their binary mixing enthalpy of liquid and the atomic radii are shown in table 3.1 [37, 38]. Furthermore, equiatomic senary $(CuNiBe)_{50}(ZrTiHf)_{50}$ alloy is reported to exhibit critical diameter of 15 mm [39]. Therefore a series of equiatomic binary to denary compositions, viz., $Cu_{50}Zr_{50}$, $(CuNi)_{50}(ZrTi)_{50}$, $(CuNiBe)_{50}(ZrTiHf)_{50}$, $(CuNiBeCo)_{50}(ZrTiHfTa)_{50}$, $(CuNiBeCoFe)_{50}(ZrTiHfTaNb)_{50}$ (in at.%) denoted as CZ2, CZ4, CZ6, CZ8, and CZ10 respectively hereafter, were selected. Their corresponding values were calculated using the following equations

$$\delta = \sqrt{\sum x_i \left(1 - \frac{r_i}{\sum x_i r_i}\right)^2} \times 100 \qquad \text{eq. 3.1}$$

$$\Delta H_{mix} = \sum_{i \neq j} 4 \Delta H_{ij}^{mix} x_i x_j \qquad \text{eq. 3.2}$$

$$S_{conf} = -R \sum x_i \ln x_i \qquad \text{eq. 3.3}$$

Where, x_i is the mole fraction, r_i is the atomic radius of the i^{th} element, ΔH_{ij}^{mix} is the mixing enthalpy of liquid in i^{th} & j^{th} binary system and R is the universal gas constant. The calcaulted values are listed in the table 4.2. As shown in the Fig. 3.1, δ (multiplied by 100 for convenience) and the ΔH_{mix} values of the alloys are close to each other with 11.5±1.3 and 27±5 kJ/mol, respectively, whereas S_{conf} monotonically increases from 5.76 J/K·mol for CZ2 to 19.14 J/K·mol for CZ10. As stratized, it can be noted that this series of alloys enables us to investigate the influence of S_{conf} on the GFA and the mechanical responses under controlled ΔH_{mix} and δ condition.

Table 3.1. Binary system mixing enthalpy of liquid (kJ/mol) [38] and atomic radii (nm) [37] of considered elements in this study. The atomic radii are shown on the diagonal positions.

Element	Cu	Ni	Be	Co	Fe	Zr	Ti	Hf	Ta	Nb
Cu	0.128	4	0	6	13	-23	-9	-17	2	3
Ni		0.125	-4	0	-2	-49	-35	-42	-29	-30
Be			0.113	-4	-4	-43	-30	-37	-24	-25
Co				0.125	-1	-41	-28	-35	-24	-25
Fe					0.124	-25	-17	-21	-15	-16
Zr						0.160	0	0	3	4
Ti							0.146	0	1	2
Hf								0.158	3	4
Ta									0.143	0
Nb										0.143

Table 3.2. δ, $\Delta \boldsymbol{H_{mix}}$, and S_{conf} calculated by eq. 3.1 to 3.3 for CZ2 to CZ10.

Alloy notation	δ	ΔH_{mix} (kJ/mol)	S_{conf} (J/K·mol)
CZ2	11.26	-23.00	5.76
CZ4	10.34	-28.00	11.53
CZ6	12.77	-31.67	14.89
CZ8	11.68	-28.44	17.29
CZ10	11.00	-24.40	19.14

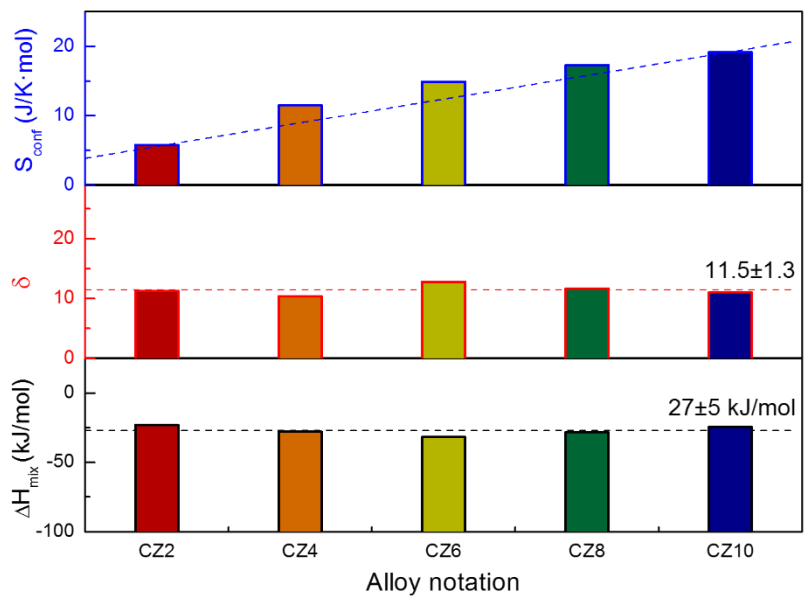

Figure 3.1. Graphs showing δ, ΔH_{mix}, and S_{conf} for CZ2 to CZ10. δ and ΔH_{mix} values fall within the range of 11.5±1.3 and 27±5 kJ/mol, respectively.

3.2. Structural analysis

Since the alloys were designed by substituting elements from $Cu_{50}Zr_{50}$ composition with topologically and chemically similar elements following the empirical rules for good glass formation, the alloys from CZ2 to CZ10 were expected to exhibit considerable GFA.

3.2.1. X-ray diffraction analysis

The results of XRD analysis is shown in Fig. 3.2, which shows broad diffraction peaks in the 2θ range of 33-47 °, an indication of an amorphous structure for all the alloys of the series. The peak positions are located within 2 ° deviation even under drastic compositional change from binary CZ2 to denary CZ10.

3.2.2. Transmission electron microscopy analysis

TEM analysis was employed to verify the amorphous nature of the amorphous nature of the as-spun samples since XRD technique has limitations in examining the presence of the crystalline precipitates of small volume fraction and size, especially those in nanoscale regime. Fig. 3.3 shows (a) a HRTEM image, (b) SAD pattern (inset: intensity profile) and (c) corresponding fast Fourier transformed (FFT) patterns obtained from the as-spun CZ10 ribbon specimen. Despite the alloy being composed of 10 elements in

equiatomic ratio, the random atomic arrangement in the HRTEM image (Fig. 3.3a), the diffuse halo ring pattern without any diffracted spot in the inset SAD pattern (Fig. 3.3b) and the FFT pattern (Fig. 3.3c) also demonstrate the fully amorphous structure with no distinguishable crystallites even on the nanometer scale. In particular, the intensity profile of the electron diffraction obtained using PASAD software (inset of Fig. 3.3b) exhibits no peaks indicative of the crystalline phase, which is in good agreement with the HRTEM image. These results show that even the new equiatomic alloy compositions bearing over eight constituent components, viz., CZ8 and CZ10, can successfully be fabricated into MG ribbon specimens by melt spinning.

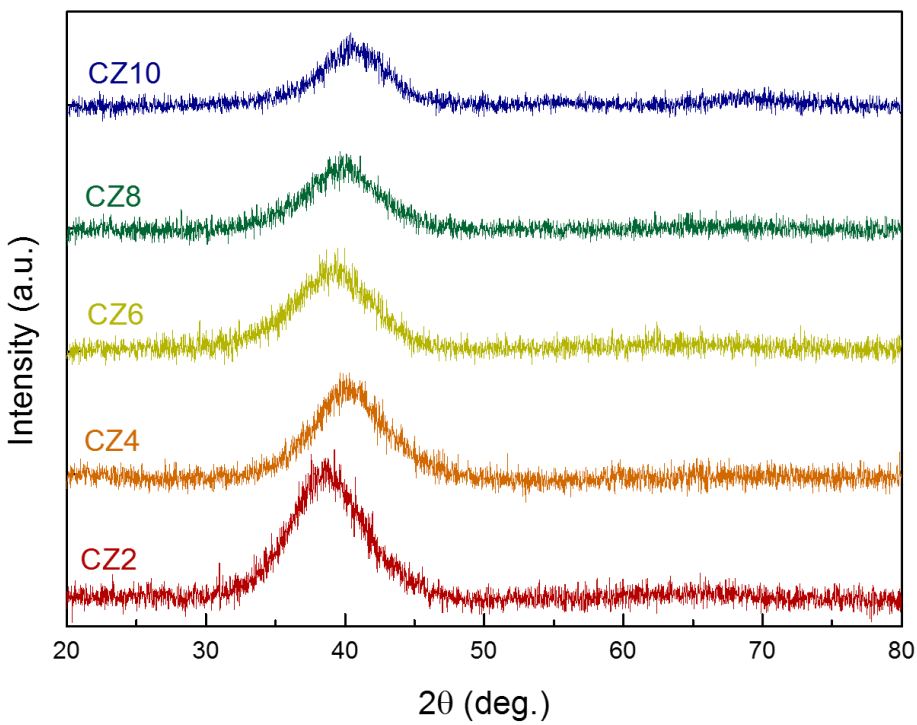

Figure 3.2. XRD patterns obtained from as-spun CZ2 to CZ10 ribbon specimens.

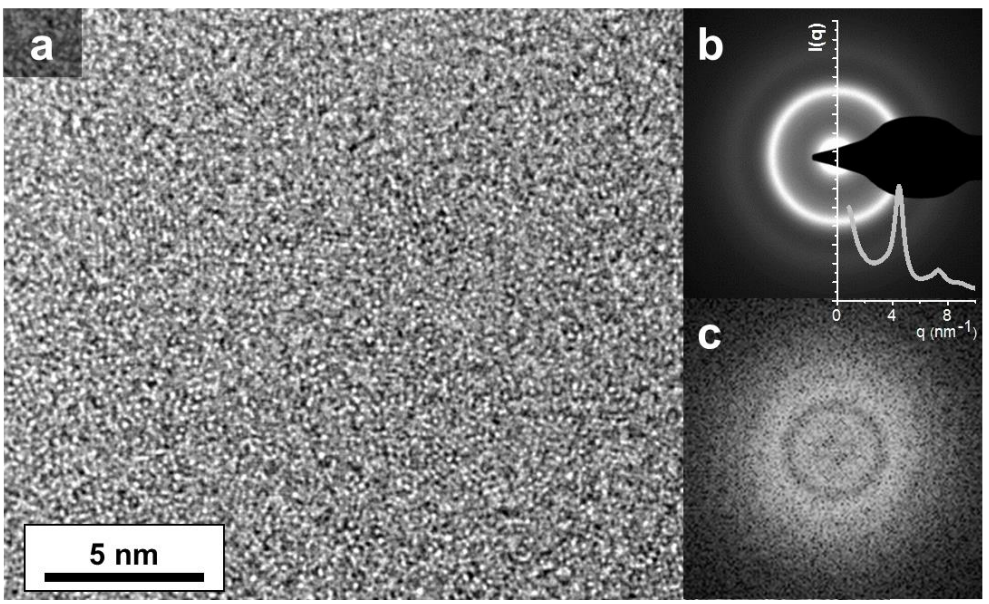

Figure 3.3. (a) HR-TEM image of as-spun CZ10 ribbon, (b) Corresponding SAD pattern, and (c) FFT pattern confirming the non-crystalline nature of the ribbon specimen.

3.2.3. High energy X-ray scattering analysis

Fig. 3.4 shows the structure factor *S(Q)* of the series of alloys under investigation in the as-spun ribbon condition obtained from the high energy XRS measurement. The shapes of the *S(Q)* curves show characteristics of glassy phases, i.e., without narrow sharp peaks occurring, exhibiting small shoulder following the second peak and the curves finally oscillating about *S(Q)* value equal to 1. These results too indicate the glassy nature of the alloys in their as-spun ribbon conditions.

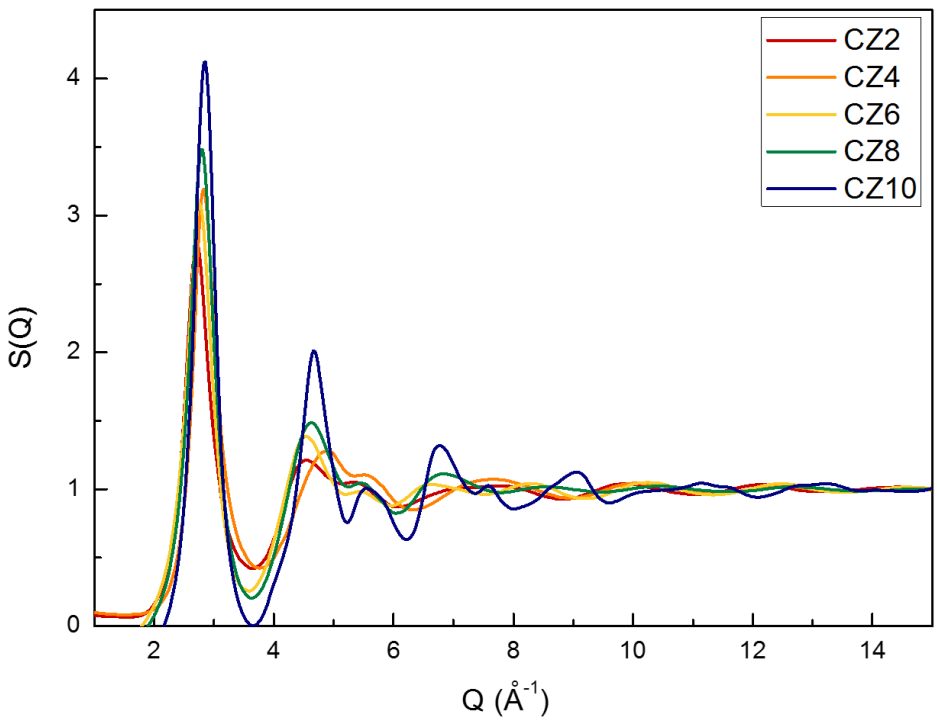

Figure 3.4. *S(Q)* of the series of investigated alloys obtained from the high energy XRS experiment.

3.3. Glass-forming ability evaluation

Fig. 3.5 shows the DSC thermograms of the CZ2 to CZ10 MGs indicated with T_g, T_x, and T_l. The measured T_g and T_x show a gradual increase along the series, which reflect on the greater metastable liquid stability and resistance to crystallization, respectively. And an increase in S_{conf} of the alloys from CZ2 to CZ10 leads to a noticeable change in normalized heat exchanges that occur during crystallization, resulting in a significant decrease in peak intensities. However, T_l initially decreases with an increase in S_{conf} from 1258 K for CZ2 to 1107 K of CZ6, and then increases up to 1498 K for CZ10. In addition, the GFA parameters introduced in the previous section 1.1.2 were calculated using the characteristic temperatures measured. The measured characteristic temperatures and the calculated GFA parameters are listed in the table 3.3. Fig. 3.6 shows the variation of calculated GFA parameters of the alloy series. As can be observed from the figure, the parameter values show a steady increase from CZ2 to CZ6 and then decrease. As already mentioned, the critical diameters of CZ2, CZ6 are 2 and 15 mm respectively. Furthermore, it was confirmed that CZ10 was not able to vitrify when casted into 1 mm rod specimen using water-cooled copper mold suction casting technique.

Confusion principle is a theory proposed by Greer in 1995 [40] wherein the GFA of the alloy improves by bearing more number of

constituent elements because of the confusion developed by the competition of feasible crystalline phases which would consequently delay the crystallization behavior when solidifying from the liquid melt. Because the alloys investigated in this study have increasing S_{conf} along the series through addition of constituent elements, we can expect that the GFA of alloys possessing higher S_{conf} values to be better due to the due to the crystallization suppression according to the confusion principle and the sluggish diffusion. However, the actuall trend of the GFA does not agree even though the alloy design involved minimizing the effect of δ and ΔH_{mix}. This shows that S_{conf} is not the dominant factor in influencing the GFA.

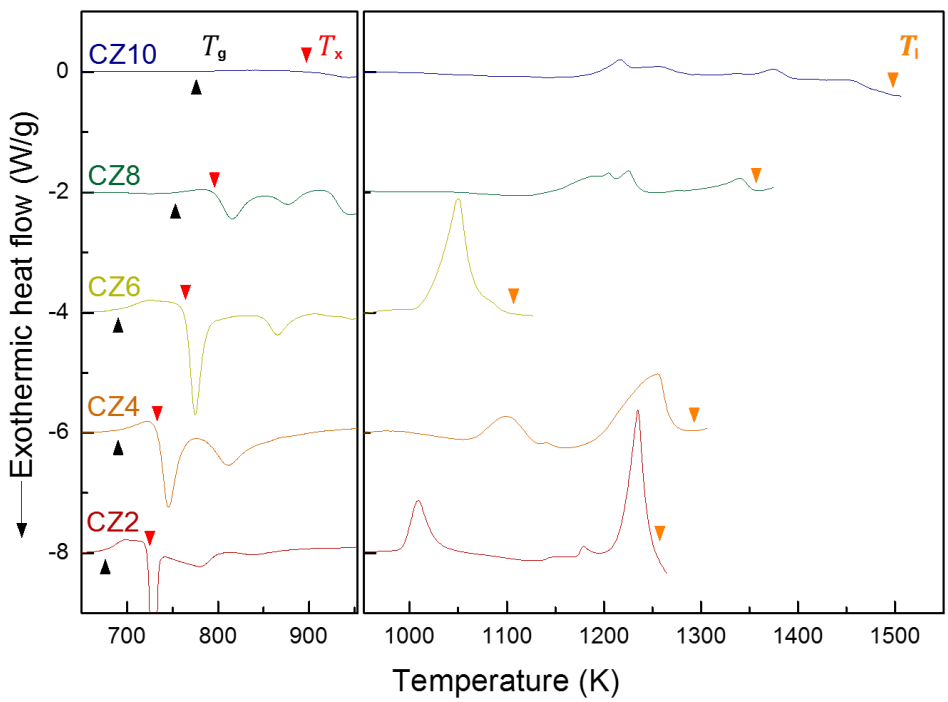

Figure 3.5. DSC traces obtained from as-spun CZ2 to CZ10 ribbons. Black, red, and orange arrow heads indicate the T_g, T_x, and T_l respectively.

Table 3.3. The characteristic temperatures (T_g, T_x, T_l, and $\boldsymbol{T_m^{mix}}$) and the calculated GFA parameters (T_{rg}, γ, and ε) for CZ2 to CZ10 MGs.

Alloy notation	T_g (K)	T_x (K)	T_l (K)	T_m^{mix} (K)	T_{rg}	γ	ε
CZ2	676	725	1258	1743	0.537	0.375	0.722
CZ4	690	733	1293	1786	0.534	0.370	0.711
CZ6	690	764	1107	1869	0.623	0.425	0.856
CZ8	753	796	1357	2034	0.555	0.377	0.745
CZ10	776	897	1498	2083	0.518	0.394	0.770

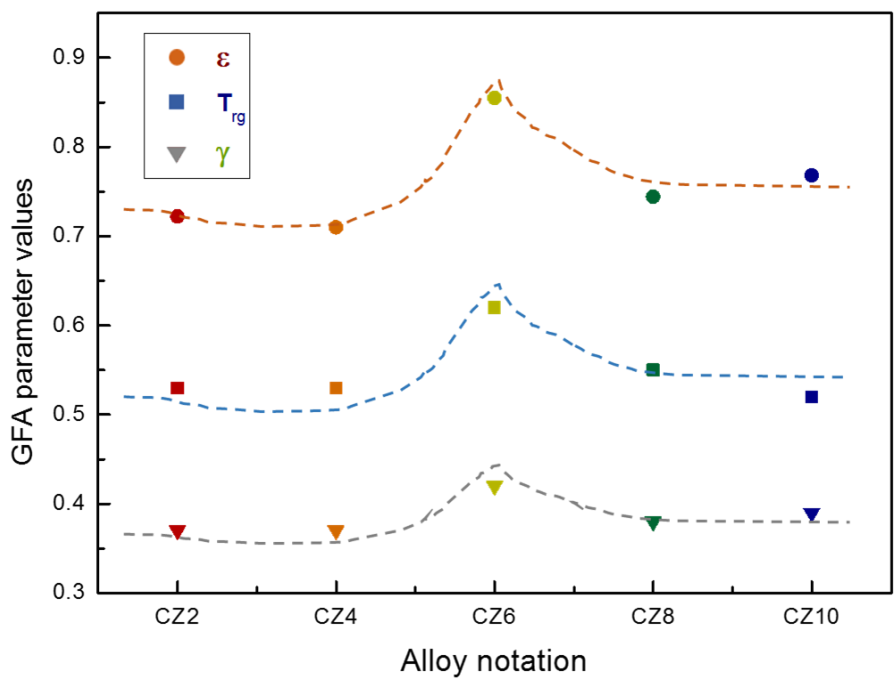

Figure 3.6. Plot showing calculated GFA parameters (T_{rg}, γ, and ε) for CZ2 to CZ10 MGs.

3.4. Fragility evaluation

To understand the structural variation due to the increment of S_{conf} from CZ2 to CZ10 MGs, we measured the dynamic fragility by analyzing the temperature dependence of relaxation time of the MGs. Fig. 3.7 shows the variation of $\ln\Phi$ a function of T_g for CZ2 to CZ10 alloys. The plots were fitted using the eq. 1.7 and the corresponding fitting parameters, $\ln A$, T_g^0 and D, obtained are also listed in the same figure. Subsequently, the fragility index, m, evaluated for the heating rate of 20 K/min of the alloys were calculated using the eq. 1.8. From the comparison of the m values, it is evident that the MGs along the series seem to become stronger glasses. This is an indication of overall structural change. It is well known that the fragility of a glass-forming liquid is intimately related to the fundamental property of the corresponding glassy phase, namely, GFA, elastic moduli, or Poisson's ratio to name a few. However, the overall linear trend between the GFA and the fragility does not hold in this series of alloys as we observe from CZ2 to CZ10. Thus, it is necessary to consider why these differences occur in this series of MGs by evaluating other relevant property changes and through detailed structural analysis.

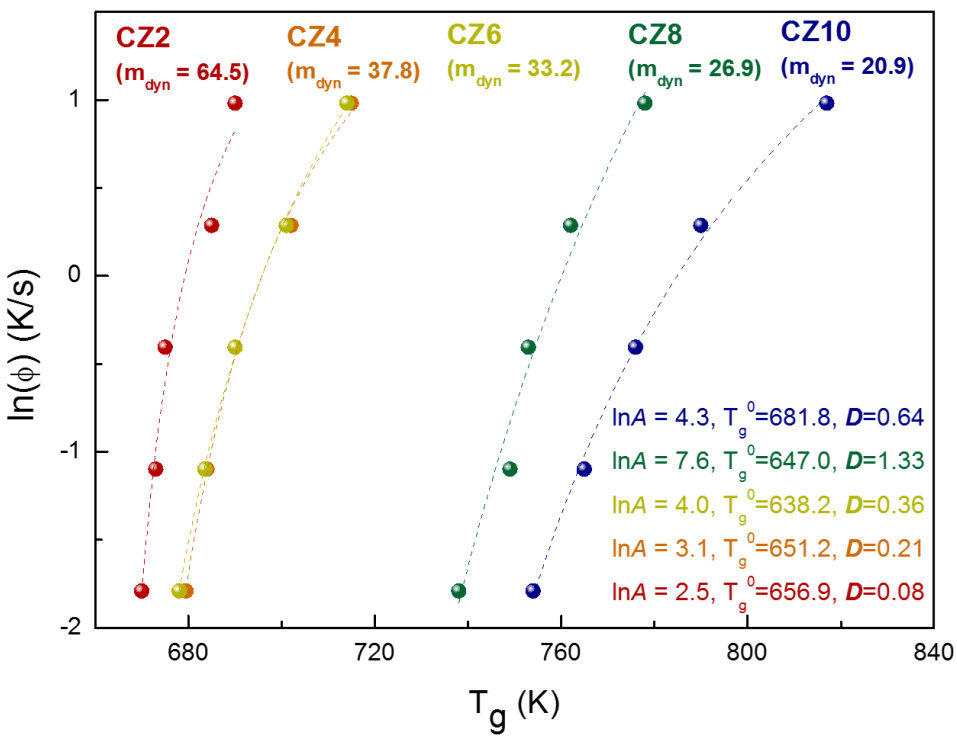

Figure 3.7. Plot showing variation of $\ln\Phi$ a function of T_g for CZ2 to CZ10.

3.5. Nanoindentation test

Even for the MGs without sufficient plasticity, the analysis of the characteristics of the intermittent shear avalanches is possible for the data obtained via nanoindentation due to the stabilization of the plastic shearing through the confinement from the surrounding matrix. Fig. 3.8 shows the load–displacemeent curves of the as–spun CZ2 to CZ10 ribbon specimens obtained from the nanoindentation test. The curves show a systematic decrease in the maximum depths along the series from binary CZ2 to denary CZ10 MG. And the mechanical properties, nanohardness and reduced Young's modulus (E_r), derived from the curves are tabulated in the table 3.4 and are plotted in the Fig. 3.9. The overall trend of the nanohardness and the E_r of the alloys along the series is shown to increase from 7.1±0.2 to 10.8±0.3 GPa and from 89.4±1.0 to 109.9±2.5 GPa respectively.

It is widely known for MGs that the hardness (Vicker's hardness, H_v) and the Young's modulus (E) are reported to be directly correlated ($H_v = E/20$) [41]. However, a close examination of the nanohardness and the E_r values of reveals an anomaly in the variation, which can clearly be observed by comparing the values of CZ4 and CZ6 as well as CZ8 and CZ10 MGs. To help visualize the differences in the tendency off those values, dotted boxes and arrows were drawn in the Fig. 3.9. The arrows indicate the direction and the magnitude of change in the property value with respect to the MGs

enclosed within the boxes. The nanohardness shows a monotonic increment pattern, whereas E_r exhibits alternating pattern with relative increment ($\Delta E_r^{\mathrm{CZ4-CZ2}}$=15.2 GPa & $\Delta E_r^{\mathrm{CZ8-CZ6}}$=14 GPa) and decrement ($\Delta E_r^{\mathrm{CZ6-CZ4}}$=−5.4 GPa & $\Delta E_r^{\mathrm{CZ10-CZ8}}$=−3.3 GPa) occurring consecutively. Thus, we can observe that even in the case of elastic modulus, the direct correlation to the fragility does not hold in this series of alloys. A detailed analysis regarding this will be discussed in the section 4.2.

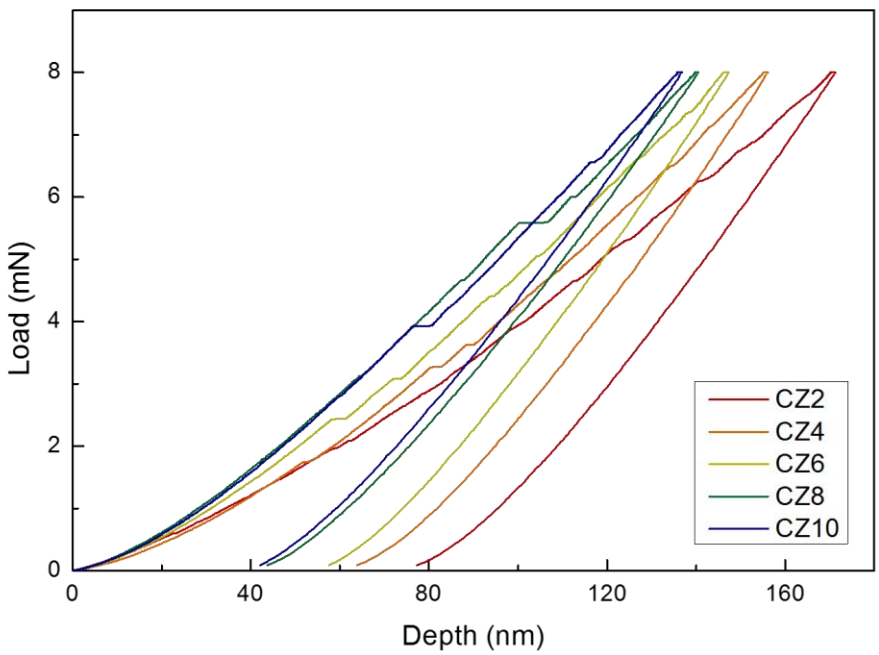

Figure 3.8. Load vs displacement curves of CZ2 to CZ10 MGs.

Table 3.4. The nanohardness and E_r obtained from the nanoindentation test.

	CZ2	CZ4	CZ6	CZ8	CZ10
Nanohardness (GPa)	7.1±0.2	8.8±0.1	9.0±0.3	10.7±0.5	10.8±0.3
E_r (GPa)	89.4±1.0	104.6±1.3	99.2±6.4	113.2±8.5	109.9±2.5

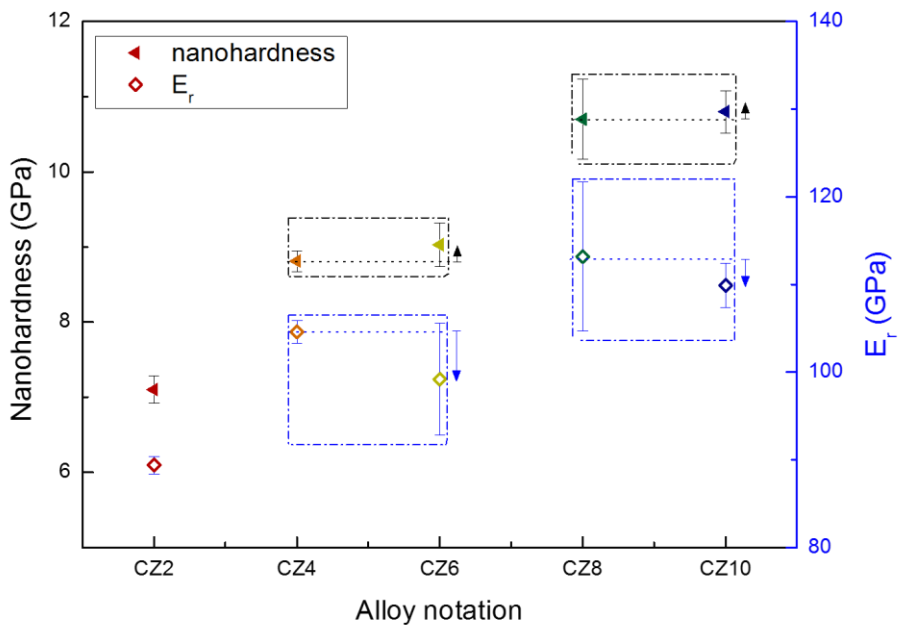

Figure 3.9. Plot showing nanohardness and E_r for CZ2 to CZ10 MGs. The arrows indicate the direction and the magnitude of the change in the property values with respect to the preceding MG enclosed within the boxes.

Chapter 4. Discussion

4.1. Influence of configuration entropy on the atomic-level structure

In general, a radial distribution function (RDF, **g(r)**) gives the distribution profile around a central atom with respect to the distance from it. Simulation techniques such as molecular dynamics yield specific atomic positions for each constituent element, allowing us to clearly decompose for each of the atomic connection types in the RDF. However, such a simulation is difficult to apply in this study due to the multicomponent nature of the alloys. Thus, we obtained **g(r)** from the total structure factor, ***S(Q)*** measured through the high energy XRS. **g(r)** can be determined through Fourier transformation of ***S(Q)*** [42]

$$g(r) = 1 + \frac{1}{2r\pi^2\rho_0}\int_0^\infty Q[S(Q)-1]\sin(Qr)dQ \qquad \text{eq. 4.1}$$

Where, ρ_0 is the average atomic number density. By normalizing the x-axis by r_1 (the first peak position or the average bond length), we can get the relative distribution profile that provides us the information about the atomic-level structure. Using molecular dynamics simulation, Ding et al. [43] have demonstrated that the second peak in the RDF of amorphous phases are characterized by the different types of atom-connection of atomic clusters or polyhedra. Consequently, specific r/r_1 ratios, $\sqrt{4}$, $\sqrt{3}$, $\sqrt{8/3}$, and $\sqrt{2}$,

in g(r) represent the most probable relative distance between the two second-nearest neighboring atoms and those values correspond to 1, 2, 3, and 4 atom-connection of polyhedra respectively. Fig. 4.1a shows the RDF curves with the x-axis normalized by their respective r_1 values. The curves corresponding to CZ2 and CZ4 MGs are very similar to each other and the position of the second peak seems to close $\sqrt{3}$ that is related to the 2 atom-connection by sharing an edge of the polyhedra. However, with an increase in S_{conf}, the position of the second peak systematically shifts towards $\sqrt{8/3}$ that is related to the 3 atom-connection by sharing a face of the polyhedra and clearly separates to two sub-peaks from CZ6 to CZ10. Although the exact atomic-level structure and the fractions for each of the atomic connections cannot be evaluated from the Fig. 4.1a, the near-identical curves might suggest a similar overall atomic-level structure of the corresponding MGs and the shift of the second peak might suggest an increased fraction of 3 atom-connection for the MGS with higher S_{conf}. Thus, the examined MGs can be classified into three groups by main atomic connections of polyhedra, i.e., 2-1 atom-connections for CZ2 and CZ4, 3-2 atom-connections for CZ6 and CZ8, and 3-1 atom-connections for CZ10. In particular, it can be noted that the increased fraction of 3 atom-connection in CZ10 leads to a large standard deviation of polyhedra connectivity, which is related to the severe local structural irregularity in the degree of disorder.

Fig. 4.1b schematically shows the high S_{conf} condition developed through the addition of principal elements in the present study that would give rise to a severe local compositional complexity because of the higher probability of different element atom occupying a neighboring position (probability (P) equal to 1/2 for a binary system, and P equal to 9/10 for a denary system) as depicted in the Fig. 4.2 even though the alloys exhibit similar δ and ΔH_{mix}. This in turn could severely distort the atomic clusters owing to different chemical nature and bond lengths apart from the difference in the atomic sizes, possibly restricting connection of more atomic clusters with severe deviation of polyhedra connections, which can be identified with a distinct separation of second sub−peak in Fig. 4.1a. Thus it can be understood that the more severe local compositional complexity as well as structural irregularity in MGs with higher S_{conf} enhances the local structural instability via distortion of atomic clusters.

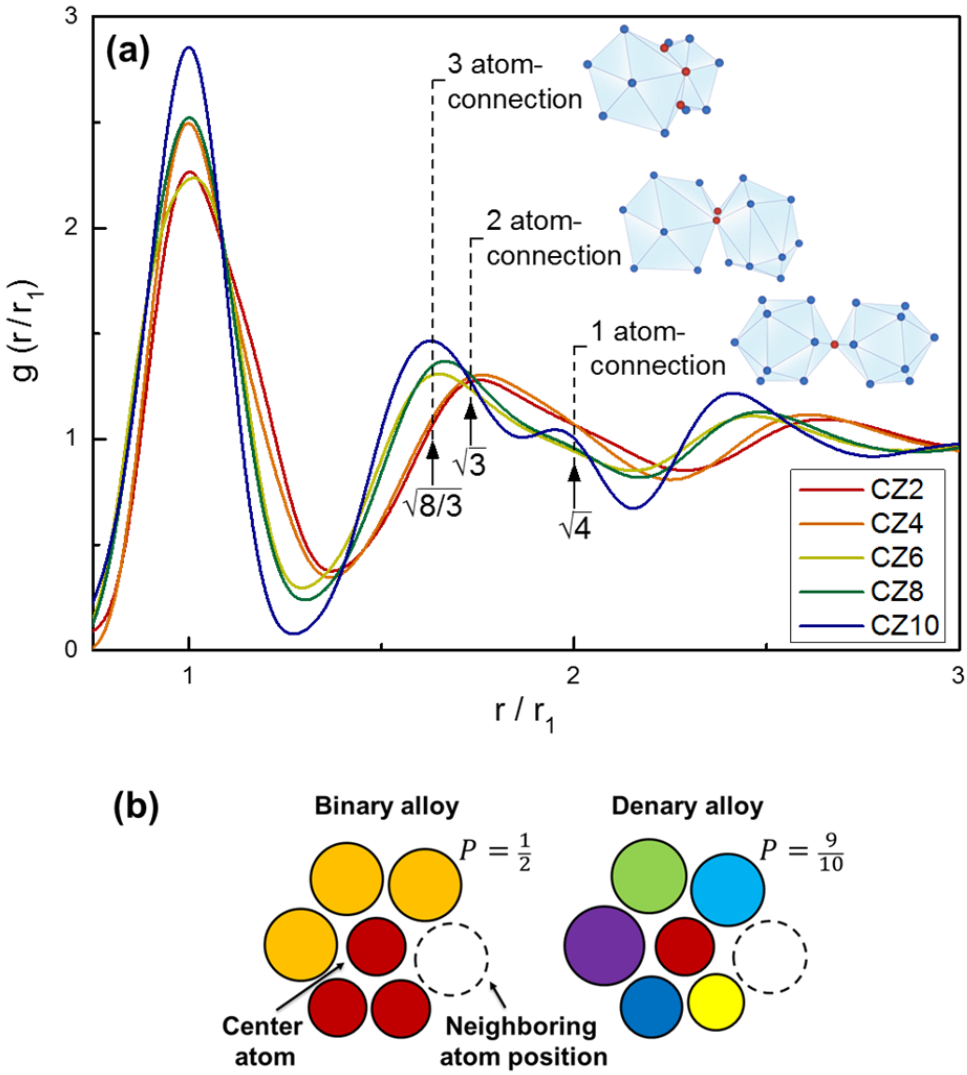

Figure 4.1. (a) Plot of g(r) normalized by the first peak position (r_1) for CZ2 to CZ10 MGs. The r/r_1 values $\sqrt{4}$, $\sqrt{3}$, $\sqrt{8/3}$ represent the 1, 2, and 3 atom−connection of polyhedra respectively. (b) Schematic diagram of binary and denary MGs indicating the probabilities of dissimilar constituent element atom occupying the neighboring atomic position giving rise to severe local compositional complexity.

Binary

	A	B
A	AA	AB
B	BA	BB

1/2

Ternary

	A	B	C
A	AA	AB	AC
B	BA	BB	BC
C	CA	CB	CC

1/3

Quaternary

	A	B	C	D
A	AA	AB	AC	AD
B	BA	BB	BC	BD
C	CA	CB	CC	CD
D	DA	DB	DC	DD

1/4

...

Denary

	A	B	C	D	E	F	G	H	I	J
A	AA	AB	AC	AD	AE	AF	AG	AH	AI	AJ
B	BA	BB	BC	BD	BE	BF	BG	BH	BI	BJ
C	CA	CB	CC	CD	CE	CF	CG	CH	CI	CJ
D	DA	DB	DC	DD	DE	DF	DG	DH	DI	DJ
E	EA	EB	EC	ED	EE	EF	EG	EH	EI	EJ
F	FA	FB	FC	FD	FE	FF	FG	FH	FI	FJ
G	GA	GB	GC	GD	GE	GF	GG	GH	GI	GJ
H	HA	HB	HC	HD	HE	HF	HG	HH	HI	HJ
I	IA	IB	IC	ID	IE	IF	IG	IH	II	IJ
J	JA	JB	JC	JD	JE	JF	JG	JH	JI	JJ

1/10

Figure 4.2. Progressive tables showing the element–element bonding in equiatomic MGs. The solvent–solvent bonding is marked with in blue background. The numbers below the table indicate respective solvent–solvent bonding probability assuming ideal random mixing.

4.2. Anomalous modulus variation in high entropy metallic glass

In glassy alloys, investigating the mechanical response is one of the effective ways to qualitatively analyze the local structural variation. To better understand the anomalous results of the nanoindentation test, the Young's moduli (E) of the MGs were calculated using the equation proposed by Wang [44]

$$\frac{1}{M} = \sum \left(f_i \cdot \frac{1}{M_i} \right) \qquad \text{eq. 4.2}$$

Where, M is the elastic constant of the MG, f_i is the fraction of the element i, and M_i is the elastic constant of the element i [45]. To further scrutinize the difference between the experimental and the calculated elastic moduli, E_r was converted to E using the relation given below

$$\frac{1}{E_r} = \frac{(1-\nu^2)}{E} + \frac{(1-\nu_i^2)}{E_i} \qquad \text{eq. 4.3}$$

Where, E_i is the Young's modulus of the indenter, ν_i is the Poisson's ratio of the indenter, and ν is the Poisson's ratio of the material. Since a diamond indenter was used, the values of E_i and ν_i were taken as 1141 GPa and 0.07 respectively [46]. The conversion was done by considering the Poisson's ratio of the MGs as 0.34, an average value of 83 compositions from the supplementary of the reference [47], except for CZ2 MG whose Poisson's ratio was

already reported as 0.36 [44]. E and G obtained by using the eq. 4.2 along with the converted E values from the measured E_r are listed in the table 4.1. Fig. 4.3a shows the variation of calculated moduli, E and G, of the alloys. It can be noticed that the tendency of increment of the calculated moduli is similar to that of the nanohardness, i.e., the calculated E and G monotonically increase. Since the overall property of the MGs is primarily influenced by the constituent elements, the enhancement of the nanohardness and E in MGs with higher S_{conf} seems reasonable due to the substitution of the pre-constituent elements with elements possessing better inherent mechanical properties. However, as shown in the Fig. 4.3b, the difference between the calculated and the measured E values for CZ2 MG is 5.0±1.0 GPa, which keep increasing up to 22.8±2.7 GPa for CZ10 MG. In other words, as S_{conf} of the system increases in the series of CZ2 to CZ10, the alloy with higher S_{conf} seems to exhibit lower E values compared to the predicted values which have been derived solely from the elemental modulus values. Eq. 4.2 is based on the previous observation that the various properties of MGs including the elastic property, plasticity, and T_g are principally determined (inherited) from the average of the intrinsic properties of the solvent or the base element [48]. The deviation occurring in HE-MGs implies the loss of the inheritance.

Two approaches are conceivable for explanining the deviation of moduli of HE-MGs. First, the amount of the solvent-solvent

bonded cluster may decrease with increasing S_{conf}. As schematically described in Fig. 4.2, the fraction of the same element bonding (such as A−A, or B−B) is inversely proportional to the number of principal elements and consequently to the S_{conf}, assuming random ideal mixing. The solvent−solvent bonded cluster provides the weakest junction in MGs, where the elastic deformation mainly occurs [48, 49], which is the physical origin of the inheritance of mechanical properties. Second, Cheng and Ma [50] have reported that the structural ordering within the glassy phase influences the elastic modulus of MGs. In the reference, higher S_{conf} condition (achieved via faster cooling rate) decreased the fraction and the connectivity of the full icosahedra, ultimately lowering the shear modulus.

Table 4.1. Calculated moduli (E and G) and measured E of CZ2 to CZ10 MGs.

Alloy notation	Calculated E (GPa)	Calculated G (GPa)	Measured E (GPa)
CZ2	89.3	39.1	84.3±1.0
CZ4	111.1	46.0	101.8±1.4
CZ6	114.4	46.8	96.1±7.0
CZ8	128.0	51.4	111.2±9.4
CZ10	130.3	51.5	107.5±2.7

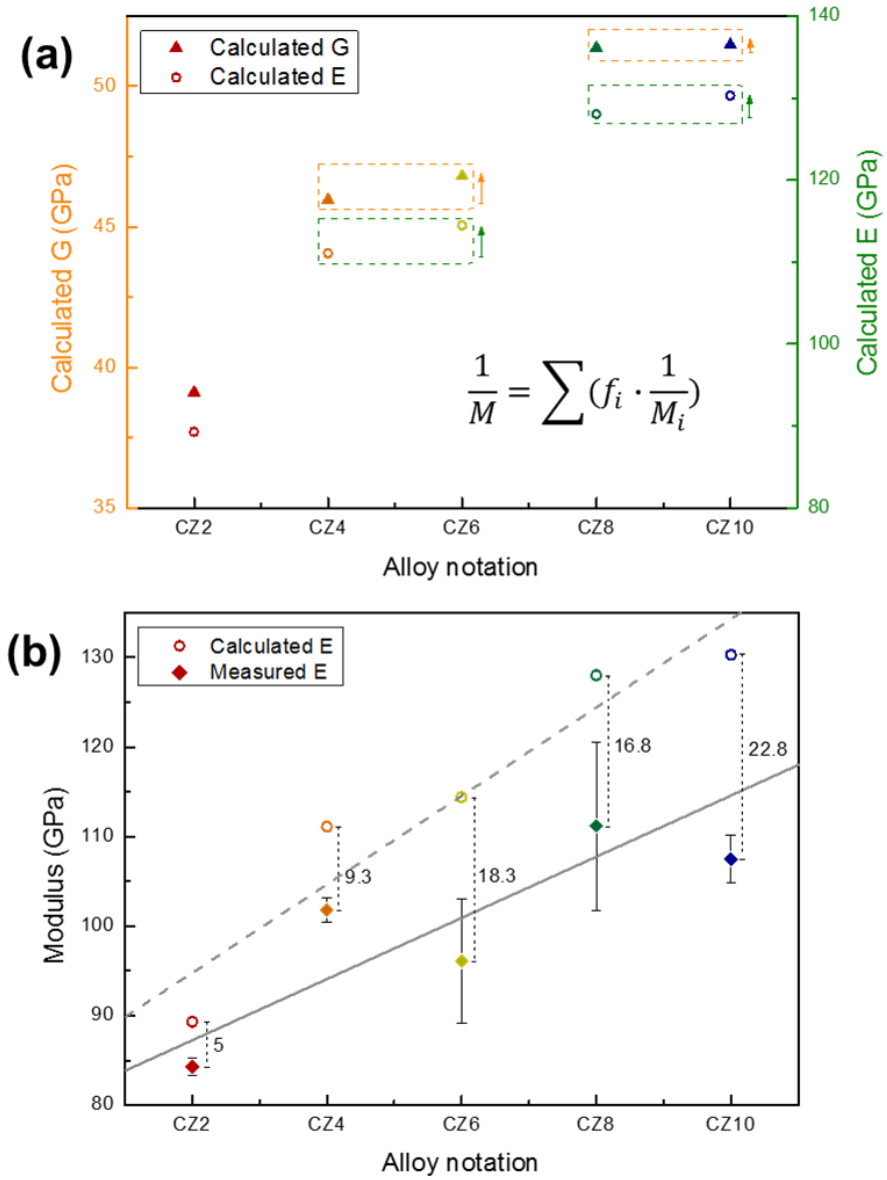

Figure 4.3. Plots showing (a) calculated E & G, and (b) calculated & measured E for CZ2 to CZ10 MGs. The arrows indicate the direction and magnitude of change in the property value with respect to the preceding MG enclosed within the boxes. In (b), the grey dotted and the solid lines represent the linear fits of the calculated and the measured E respectively.

4.3. Anomalous deformation dynamics of high entropy metallic glass

To observe the changes in the characteristic behavior from CZ2 to CZ10, statistical analysis of shear avalanches was carried out with the pop-ins collected from the processed nanoindentation data. A second degree polynomial function was used to fit the loading part in the load-displacement curve to get a baseline which was subtracted from the original loading curve, indicated by Δh_s $(=h_{exp} - h_{fit})$. This way, the influence of the indentation depth was eliminated, enabling us to identify the pop-ins better. The pop-ins, Δh, were distinguished by selecting the difference in the height between the peak and the valley above a threshold noise level (obtained using an algorithm on the holding curve). Fig. 4.4a, c, and e shows Δh_s as a function of the depth (h) for a single indentation for CZ2, CZ6, and CZ10. The results indicate a simultaneous occurrence of reduction in the number and the increment in the magnitude of Δh for a single indentation performed as the MGs possess higher $S_{conf.}$ As a corollary, the increasing pop-in size occurring over a wide range of depths along the series can easily be seen by comparing the pop-in size vs depth plots for multiple indentations in Fig. 4.4b, d, and f. This change in the mechanical response is due to the transition from unjamming to jamming state of concordant regions along this series of MGs.

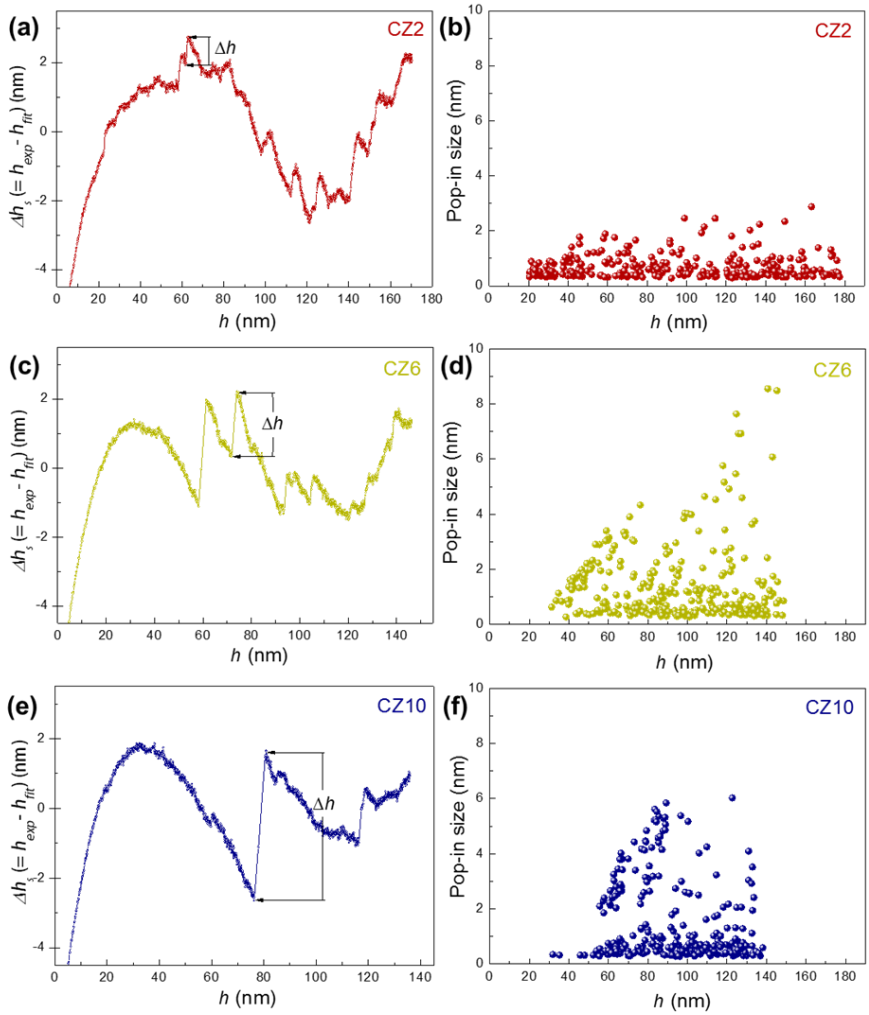

Figure 4.4. (a), (c), and (e) showing the plot of subtracted depth ($\Delta h_s = h_{exp} - h_{fit}$) vs depth ($h$) for a single indentation for CZ2, CZ6, and CZ10 MGs respectively. (b), (d), and (f) show the distribution of pop-in size (Δh) as a function of h for CZ2, CZ6, and CZ10 MGs respectively.

After the calculation of strain burst sizes ($S=\Delta h/h$), cumulative probability distribution function, $P(>S)$, was used to fit the distribution to the following empirical relation [17]

$$P(>S) = AS^{-(\kappa-1)} \exp\left(-\left(\frac{S}{S_c}\right)^2\right) \qquad \text{eq. 4.4}$$

Where, A is a normalization constant, κ is a scaling exponent, and S_c is the cut-off strain burst size at which an exponentially decaying behavior begins from the power-law relation. Fig. 4.5 shows the cumulative probability distribution of strain burst sizes for the series of alloys along with the correspondingly colored power-law fitted solid lines and S_c indicated by the arrow heads, which show power-law scaling behavior in small S regime, and truncation at large S regime. Table 4.2 lists κ and S_c values of CZ2 to CZ10 MGs. It was reported that a system that exhibits SOC behavior more dominantly will possess larger S_c. On the contrary, a system that shows dominant chaotic shear avalanche possesses smaller S_c. As it can be observed, S_c steadily increases in the series from 0.0202 for CZ2 to 0.0419 for CZ6 and finally to 0.0625 for CZ10 MG, indicating chaotic to SOC behavior transition with increasing S_{conf}.

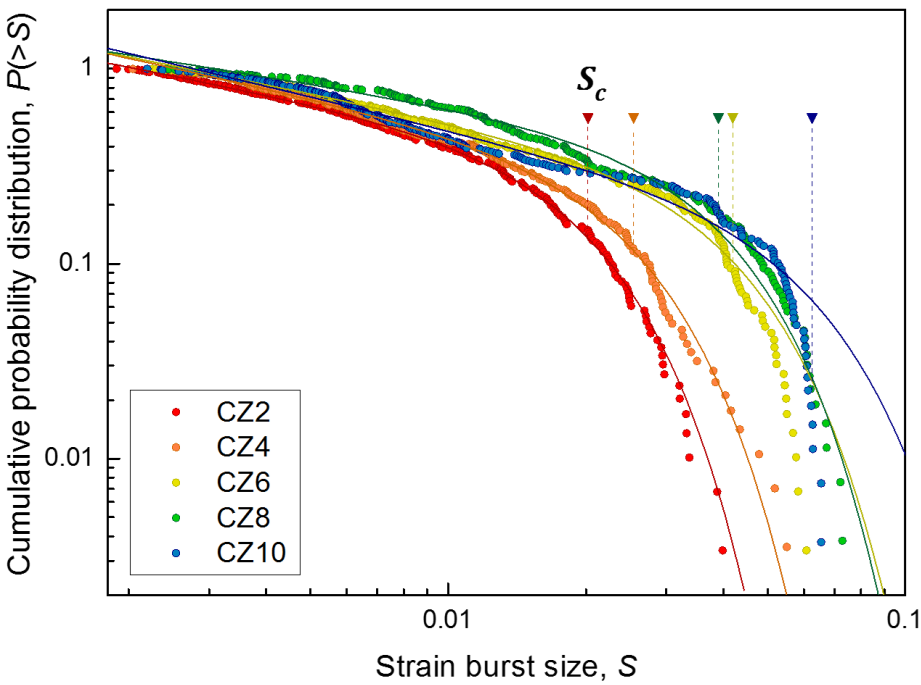

Figure 4.5. Cumulative probability distribution of strain burst sizes of the investigated alloy series. Solid scattering points represent the experimental results obtained from the nanoindentation and solid lines are the attained fittings of each distribution using eq. 4.4. The arrow heads mark the corresponding S_c.

Table 4.2. κ and S_c values of the MGs obtained through the fitting using eq. 4.4.

Alloy notation	κ	S_c
CZ2	1.46	0.0202
CZ4	1.48	0.0254
CZ6	1.45	0.0419
CZ8	1.36	0.0390
CZ10	1.55	0.0625

Fig. 4.6a–e shows the histograms collected from the series of nanoindentation tests in the MGs. The dotted lines signify the respective S_c whereas the solid curves represent the strain burst size distribution profiles obtained from the power–law fittings. It can clearly be understood that the large strain burst sizes occur for MGs with higher S_{conf} of the alloy series which is in good agreement with the higher S_c values. Fig. 4.6f shows the plot of κ and S_c values for the series of alloys. The κ values are within the range of 1.46±0.1, close to the mean field value of 1.5 [51], an evidence of randomly packed amorphous state. Previous studies reported higher S_c values for harder MGs [8, 14]. This is reasonable since harder MGs are able to withstand harsher stress condition consequently maintaining SOC behavior, resulting in higher S_c values. Indeed, even in this work, the harder MGs showed higher S_c values as reported. However, it is interesting to note that CZ2, CZ4 and CZ6, CZ8 pairs show analogous slip avalanche behavior and small difference of corresponding S_c values ($\Delta S_c^{CZ4-CZ2}$ =0.0052 and $\Delta S_c^{CZ8-CZ6}$ =−0.0029) despite the significant nanohardness difference ($\Delta\text{nanohardness}^{CZ4-CZ2}$=1.7 GPa and $\Delta\text{nanohardness}^{CZ8-CZ6}$ =1.7 GPa). In detail, the severe local structural irregularity and the compositional complexity in MG with higher S_{conf} seems to influence the S_c, by promoting the manifestation of SOC behavior due to the aforementioned distortion of the atomic clusters, which results in the unexpected local softening by weakened jammed state of shear transformation zones, and

ultimately modulating the response towards the ductile mechanical deformation. Thus, an effective alloy design utilizing the influence of S_{conf} to tune the properties could be applied to develop MGs possessing adequate GFA and considerable ductility. However, further investigation is necessary to deduce precise contribution to the properties.

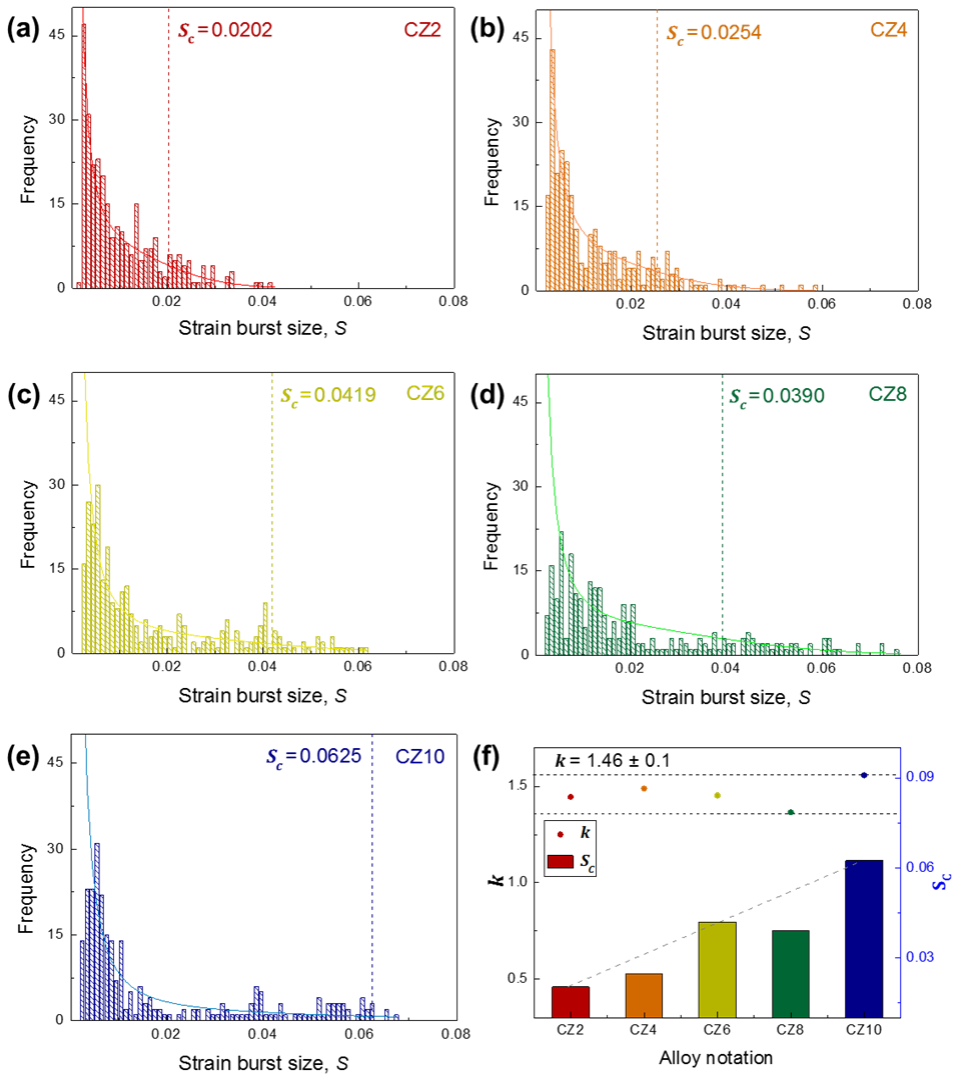

Figure 4.6. histograms plotted from the nanoindentation tests for (a) CZ2, (b) CZ4, (c) CZ6, (d) CZ8, (e) CZ10. The bin size used is 10^{-3}. (f) plot comparing the values of κ and S_c. The values of κ are within the range of 1.46±0.1, which are close to the mean field value of 1.5.

Chapter 5. Conclusion

This study emphasizes on the effect of S_{conf} on the GFA and the mechanical responses in a series of equiatomic binary to denary alloy under the minimized deivation of δ and ΔH_{mix} among the alloys. The higher S_{conf} in this study caused improved overall amorphous phase stability (increased fraction of 3 atom−connection of polyhedra and lower fragility index), but simultaneously increased the severe local structural instability (increased deviation of polyhedra connectionvity and decreased solvent−solvent bonding probability leading to the loss of MG' s property inheritance), which resulted in anomalous GFA and the mechanical responses (elastic moduli and deformation dynamics). First, the senary CZ6 MG with medium S_{conf} of $1.79R$ exhibits maximum GFA among the series of alloys, implying that the higher S_{conf} is not a sufficient condition for achieving higher GFA. The senary CZ6 alloy also exhibits the largest relative decrease of melting temperature (ΔT^*=0.41) and the highest GFA parameters (T_{rg}=0.623, γ=0.425 and ε=0.856), which is related to the longest onset time of nose point of C−curve and consequently has the lowest critical cooling rate within the series of investigated MGs. Second, the overall trend of nanohardness and E from CZ2 to CZ10 MGs is shown to outwardly increase which is dominantly due to the increased 3 atom−connection of polyhedra as well as lower fragility index. However, if we carefully analyze, the relationship between the

elastic moduli and the fragility index does not hold in this series of alloys due to the occurrence of alternating increment and decrement of E_r and lower measured E with widening deviation from calculated E. In particular, considering the similar overall atomic-level structure of CZ2 & CZ4, and CZ6 & CZ8 and the relatively large difference in the nanohardness (1.7 GPa in both the cases), the change in S_c is abnormally small, indicating a low rate of increment of S_c, facilitation of chaotic behavior of shear avalanche. The manifestation of these results can be attributed to the severe local compositional complexity (related to the low solvent-solvent bonding probability and loss of property inheritance) and the structural irregularity (deduced from the increased deviation of polyhedra connectivity) in MGs with higher S_{conf} ultimately leading to the local softening of the amorphous phase, modulating the response towards the ductile deformation. Hence, it can be concluded that the S_{conf} could be one of the crucial factors in designing a MG in order to tune the vital properties for engineering application.

Bibliography

[1] C. Suryanarayana, A. Inoue, Bulk metallic glasses, 2nd ed., CRC Press2017.

[2] A. Inoue, Stabilization of metallic supercooled liquid and bulk amorphous alloys, Acta materialia 48(1) (2000) 279-306.

[3] J. Kim, Fabrication and mechanical response of nanoscale metallic glasses, Department of materials science and engineering, Seoul National University, 2016.

[4] D. Turnbull, Under what conditions can a glass be formed?, Contemporary physics 10(5) (1969) 473-488.

[5] Z. Lu, C. Liu, A new approach to understanding and measuring glass formation in bulk amorphous materials, Intermetallics 12(10-11) (2004) 1035-1043.

[6] E. Park, C. Ryu, W. Kim, D. Kim, A novel parameter to describe the glass-forming ability of alloys, Journal of Applied Physics 118(6) (2015) 064902.

[7] C.A. Angell, Formation of glasses from liquids and biopolymers, Science 267(5206) (1995) 1924-1935.

[8] J. Kim, H.S. Oh, J. Kim, C.W. Ryu, G.W. Lee, H.J. Chang, E.S. Park, Utilization of high entropy alloy characteristics in Er-Gd-Y-Al-Co high entropy bulk metallic glass, Acta Materialia 155 (2018) 350-361.

[9] A. Greer, Y. Cheng, E. Ma, Shear bands in metallic glasses,

Materials Science and Engineering: R: Reports 74(4) (2013) 71-132.

[10] A. Argon, Plastic deformation in metallic glasses, Acta metallurgica 27(1) (1979) 47-58.

[11] C.A. Schuh, T.C. Hufnagel, U. Ramamurty, Mechanical behavior of amorphous alloys, Acta Materialia 55(12) (2007) 4067-4109.

[12] C.A. Schuh, A.C. Lund, Atomistic basis for the plastic yield criterion of metallic glass, Nature materials 2(7) (2003) 449.

[13] R. Maaß, D. Klaumünzer, J.F. Löffler, Propagation dynamics of individual shear bands during inhomogeneous flow in a Zr-based bulk metallic glass, Acta Materialia 59(8) (2011) 3205-3213.

[14] X. Bian, G. Wang, K. Chan, J. Ren, Y. Gao, Q. Zhai, Shear avalanches in metallic glasses under nanoindentation: Deformation units and rate dependent strain burst cut-off, Applied Physics Letters 103(10) (2013) 101907.

[15] B.A. Sun, H.B. Yu, W. Jiao, H.Y. Bai, D.Q. Zhao, W.H. Wang, Plasticity of ductile metallic glasses: a self-organized critical state, Physics Review Letter 105(3) (2010) 035501.

[16] B. Sun, S. Pauly, J. Tan, M. Stoica, W.H. Wang, U. Kühn, J. Eckert, Serrated flow and stick–slip deformation dynamics in the presence of shear-band interactions for a Zr-based metallic glass, Acta Materialia 60(10) (2012) 4160-4171.

[17] X. Bian, G. Wang, H. Chen, L. Yan, J. Wang, Q. Wang, P. Hu, J. Ren, K. Chan, N. Zheng, Manipulation of free volumes in a metallic glass through Xe-ion irradiation, Acta Materialia 106 (2016) 66-77.

[18] W. Kim, H. Oh, E. Park, Manipulation of thermal and mechanical stability by addition of multiple equiatomic rare-earth elements in Al-TM-RE metallic glasses, Intermetallics 91 (2017) 8-15.

[19] J.W. Yeh, S.K. Chen, S.J. Lin, J.Y. Gan, T.S. Chin, T.T. Shun, C.H. Tsau, S.Y. Chang, Nanostructured high-entropy alloys with multiple principal elements: novel alloy design concepts and outcomes, Advanced Engineering Materials 6(5) (2004) 299-303.

[20] B. Cantor, I. Chang, P. Knight, A. Vincent, Microstructural development in equiatomic multicomponent alloys, Materials Science and Engineering: A 375 (2004) 213-218.

[21] B.S. Murty, J.W. Yeh, S. Ranganathan, High-entropy alloys, 1st ed., Butterworth-Heinemann2014.

[22] F. Otto, A. Dlouhý, C. Somsen, H. Bei, G. Eggeler, E.P. George, The influences of temperature and microstructure on the tensile properties of a CoCrFeMnNi high-entropy alloy, Acta Materialia 61(15) (2013) 5743-5755.

[23] M.A. Hemphill, T. Yuan, G. Wang, J. Yeh, C. Tsai, A. Chuang, P. Liaw, Fatigue behavior of Al0. 5CoCrCuFeNi high entropy alloys, Acta Materialia 60(16) (2012) 5723-5734.

[24] Y. Zhang, T.T. Zuo, Z. Tang, M.C. Gao, K.A. Dahmen, P.K. Liaw, Z.P. Lu, Microstructures and properties of high-entropy alloys, Progress in Materials Science 61 (2014) 1-93.

[25] Y. Zhang, Y.J. Zhou, J.P. Lin, G.L. Chen, P.K. Liaw, Solid-solution phase formation rules for multi-component alloys, Advanced

Engineering Materials 10(6) (2008) 534-538.

[26] A. Takeuchi, N. Chen, T. Wada, Y. Yokoyama, H. Kato, A. Inoue, J. Yeh, Pd20Pt20Cu20Ni20P20 high-entropy alloy as a bulk metallic glass in the centimeter, Intermetallics 19(10) (2011) 1546-1554.

[27] Y. Tong, J. Qiao, C. Zhang, J.-M. Pelletier, Y. Yao, Mechanical properties of Ti16. 7Zr16. 7Hf16. 7Cu16. 7Ni16. 7Be16. 7 high-entropy bulk metallic glass, Journal of Non-Crystalline Solids 452 (2016) 57-61.

[28] M. Yang, X. Liu, H. Ruan, Y. Wu, H. Wang, Z. Lu, High thermal stability and sluggish crystallization kinetics of high-entropy bulk metallic glasses, Journal of Applied Physics 119(24) (2016) 245112.

[29] H.F. Li, X.H. Xie, K. Zhao, Y.B. Wang, Y.F. Zheng, W.H. Wang, L. Qin, In vitro and in vivo studies on biodegradable CaMgZnSrYb high-entropy bulk metallic glass, Acta biomaterialia 9(10) (2013) 8561-73.

[30] T. Qi, Y. Li, A. Takeuchi, G. Xie, H. Miao, W. Zhang, Soft magnetic Fe25Co25Ni25 (B, Si) 25 high entropy bulk metallic glasses, Intermetallics 66 (2015) 8-12.

[31] C. Gammer, C. Mangler, C. Rentenberger, H. Karnthaler, Quantitative local profile analysis of nanomaterials by electron diffraction, Scripta Materialia 63(3) (2010) 312-315.

[32] A. Hammersley, S. Svensson, A. Thompson, Calibration and correction of spatial distortions in 2D detector systems, Nuclear Instruments

Methods in Physics Research Section A: Accelerators, Spectrometers, Detectors and Associated Equipment 346(1-2) (1994) 312-321.

[33] X. Qiu, J.W. Thompson, S.J. Billinge, PDFgetX2: a GUI-driven program to obtain the pair distribution function from X-ray powder diffraction data, Journal of Applied Crystallography 37(4) (2004) 678-678.

[34] Korea Institute of Science and Technology, Equipment, TEM. https://aac.kist.re.kr:8443/equipment/view?xmrCd=1030, 2019).

[35] Micro Mechanics & Materials Processing Design Lab., Facilities, Nano-indenter. http://mmmpdl.snu.ac.kr/?cat=15, 2019).

[36] W. Wang, J. Lewandowski, A. Greer, Understanding the glass-forming ability of Cu 50 Zr 50 alloys in terms of a metastable eutectic, Journal of materials research 20(9) (2005) 2307-2313.

[37] O. Senkov, D. Miracle, Effect of the atomic size distribution on glass forming ability of amorphous metallic alloys, Materials Research Bulletin 36(12) (2001) 2183-2198.

[38] A. Takeuchi, A. Inoue, Classification of bulk metallic glasses by atomic size difference, heat of mixing and period of constituent elements and its application to characterization of the main alloying element, Materials Transactions 46(12) (2005) 2817-2829.

[39] H. Ding, Y. Shao, P. Gong, J. Li, K. Yao, A senary TiZrHfCuNiBe high entropy bulk metallic glass with large glass-forming ability, Materials letters 125 (2014) 151-153.

[40] A.L. Greer, Metallic glasses, Science 267(5206) (1995) 1947-1953.

[41] W. Wang, Elastic moduli and behaviors of metallic glasses, Journal of Non-Crystalline Solids 351(16-17) (2005) 1481-1485.

[42] T. Egami, Atomic correlations in non-periodic matter, Materials Transactions, JIM 31(3) (1990) 163-176.

[43] J. Ding, E. Ma, M. Asta, R.O. Ritchie, Second-Nearest-Neighbor Correlations from Connection of Atomic Packing Motifs in Metallic Glasses and Liquids, Scientific Reports 5 (2015) 17429.

[44] W.H. Wang, Correlations between elastic moduli and properties in bulk metallic glasses, Journal of Applied Physics 99(9) (2006) 093506.

[45] WebElements. https://www.webelements.com, (accessed June.2018).

[46] W.C. Oliver, G.M. Pharr, An improved technique for determining hardness and elastic modulus using load and displacement sensing indentation experiments, Journal of materials research 7(6) (1992) 1564-1583.

[47] S. Kim, H. Oh, E. Park, A hidden variable in shear transformation zone volume versus Poisson's ratio relation in metallic glasses, APL Materials 5(10) (2017) 106105.

[48] D. Ma, A.D. Stoica, X.L. Wang, Z.P. Lu, B. Clausen, D.W. Brown, Elastic moduli inheritance and the weakest link in bulk metallic glasses, Physics Review Letter 108(8) (2012) 085501.

[49] W.H. Wang, Metallic glasses: Family traits, Nature materials 11(4) (2012) 275.

[50] Y. Cheng, E. Ma, Configurational dependence of elastic modulus of metallic glass, Physical Review B 80(6) (2009) 064104.

[51] J. Antonaglia, W.J. Wright, X. Gu, R.R. Byer, T.C. Hufnagel, M. LeBlanc, J.T. Uhl, K.A. Dahmen, Bulk metallic glasses deform via slip avalanches, Physics Review Letter 112(15) (2014) 155501.

Abstract in Korean

초 록

엔트로피 제어 비정질 형성 합금 시스템에서 비정질 형성능 및 기계적 특성 변화 고찰

이정수

서울대학교 공과대학

재료공학부

본 연구에서는 구성 엔트로피가 비정질 형성능 및 기계적 거동에 미치는 영향을 알아보기 위해 이성분계 $Cu_{50}Zr_{50}$ 부터 십성분계 $(CuNiBeCoFe)_{50}(ZrTiHfTaNb)_{50}$에 이르기 까지 다양한 금속원소들이 등가원소비로 이루어진 비정질 합금 시리즈의 기계적, 구조적 특성에 대해 분석하였다. 첨가 원소들간 원자 반경 차이, 혼합열 등의 특성이 비슷해 구성 엔트로피 효과를 확인하기 적합한 등가원소비 비정질 합금 시스템을 제조하기 위해 Cu 및 Zr과 화학적, 구조적 특성이 유사한 금속들을 선별하여 등가원소비로 첨가한 뒤 비정질 합금을 제조하였다. 특이하게도 비교적으로 중간 구성 엔트로피를 값을 ($1.79R$) 갖는 육성분계 $(CuNiBe)_{50}(ZrTiHf)_{50}$ 비정질 합금이 가장 높은 비정질 형성능을 보이며 구성 엔트로피가 비정질 형성능의 우성인자가 아닌 것을 알 수 있었다. 구성원소 개수에 따른 구성 엔트로피 변화가 기계적 거동에 미치는 영향을 확인하기 위해 나노압입 시험을 통한 pop-in

거동의 통계적 분석을 통해 수행하였으며, 이를 이해하기 위해 고에너지 X-선 산란 실험 (high energy X-ray scattering) 에 의해 얻어진 원자 단위 구조 데이터와 비교 하여 논하였다. 그 결과, 원자 클러스터 간 결합 패턴의 비율이 면결합 (3 atom-connection)으로 증가 및 fragility는 감소할수록 합금의 경도 및 탄성계수 변화는 전반적으로 증가함을 확인할 수 있었다. 또한 원소 첨가에 따른 구성 엔트로피 증가는 국부적으로 구조적 불규칙성 및 조성적 복잡성을 유발하여 chaotic 변형 거동을 촉진시켜 국부적 softening 현상이 나타나게 하였으며 궁극적으로 연성 변형에 대한 반응을 조절 시킬 수 있었다. 결과적으로, 구성 엔트로피는 최적의 비정질 형성능 및 향상된 연성과 같은 우수한 특성을 달성하기 위해 비정질 합금 설계에 중요한 요소임을 알 수 있었다.

핵심어: 비정질 금속; 구성 엔트로피; 비정질 형성능;
국부적 구조 불균일성, 기계적 반응

학번: 2017-25308